Structural Studies of Interleukin-1β, Interleukin-4, and Interleukin-8

G. Marius Clore and Angela M. Gronenborn

Laboratory of Chemical Physics, Building 5, National Institute of Diabetes and Digestive and Kidney Diseases, National Institutes of Health, Bethesda, Maryland 20892

In this review we present and discuss the structures of three cytokines, interleukin-1β, interleukin-4, and interleukin-8, in the solution and crystal states. The availability of these high-resolution structures provides a framework for understanding their mechanism of action, for relating structure to function, and for the rational design of potential agonists and antagonists. © 1993 Academic Press, Inc.

Cytokines play a key role in the regulation of the immune and inflammatory systems. A prerequisite for the full understanding of the molecular basis of the activity and mechanism of action of the cytokines is a knowledge of their three-dimensional structures. In addition, such knowledge is vital for determining the factors contributing to the different activities of various related proteins and for the rational design of agonists and antagonists. This article focuses on structural studies of three cytokines, namely, interleukin-1β, interleukin-4, and interleukin-8. Particular attention is paid to comparing the structures in the solution and crystal states.

GENERAL METHODOLOGY

There are two complementary approaches to obtaining three-dimensional structures of proteins. The first method is X-ray crystallography of single protein crystals in the solid state. Crystallography is in effect an imaging technique. The Fourier transform of the diffraction pattern obtained from a single crystal provides an electron density map of the protein, which can be interpreted to yield an atomic model (1). The second method is multidimensional nuclear magnetic resonance (NMR) spectroscopy in solution. The principal source of geometric information used in a NMR structure determination lies in short interproton distances (<5 Å) derived from nuclear Overhauser enhancement (NOE) measurements, supplemented by torsion angle restraints derived from three-bond coupling constants (2, 3). These distances are converted into a three-dimensional structure by means of computational procedures involving distance geometry and simulated annealing. For larger proteins (>100 residues), it is essential to employ three- and four-dimensional heteronuclear NMR to overcome the overlap problem associated with the large number of resonances that must be assigned (3). This necessitates the use of protein that is uniformly labeled (>95%) with ^{15}N and ^{13}C.

INTERLEUKIN-1β

Interleukin-1β (IL-1β) is a protein of 153 residues and 17.4 kDa with a wide range of biological activities, interacting with virtually every organ and tissue system in the body. IL-1β lies at the pinnacle of the cytokine cascade and its activities include B-cell activation, proliferation, and differentiation, T-cell activation and proliferation, prostaglandin and collagenase release, stimulation of interleukin-2 and c-*jun* transcription, induction of acute-phase protein synthesis, and fibroblast growth factor activity (4).

The high-resolution solution structure has been solved using three- and four-dimensional heteronuclear NMR spectroscopy on the basis of 3146 experimental NMR restraints (5), and the X-ray structure has been solved at 2 Å resolution (6, 7, 8).

The Solution Structure of Interleukin-1β

A schematic fold of IL-1β is shown in Fig. 1A, and two views of a superposition of an ensemble of 32 calculated NMR structures are provided in Figs. 1B and 1C. IL-1β resembles a tetrahedron and is composed of 12 antiparallel β-strands arranged in three pseudosymmetric topological units, each of which comprises 5 strands (Fig. 2). The strands are connected by turns, short loops, or long loops. Six strands (strands 1, 4, 5, 8, 9, and 12) form a β-barrel which is closed off at the back of the molecule by the
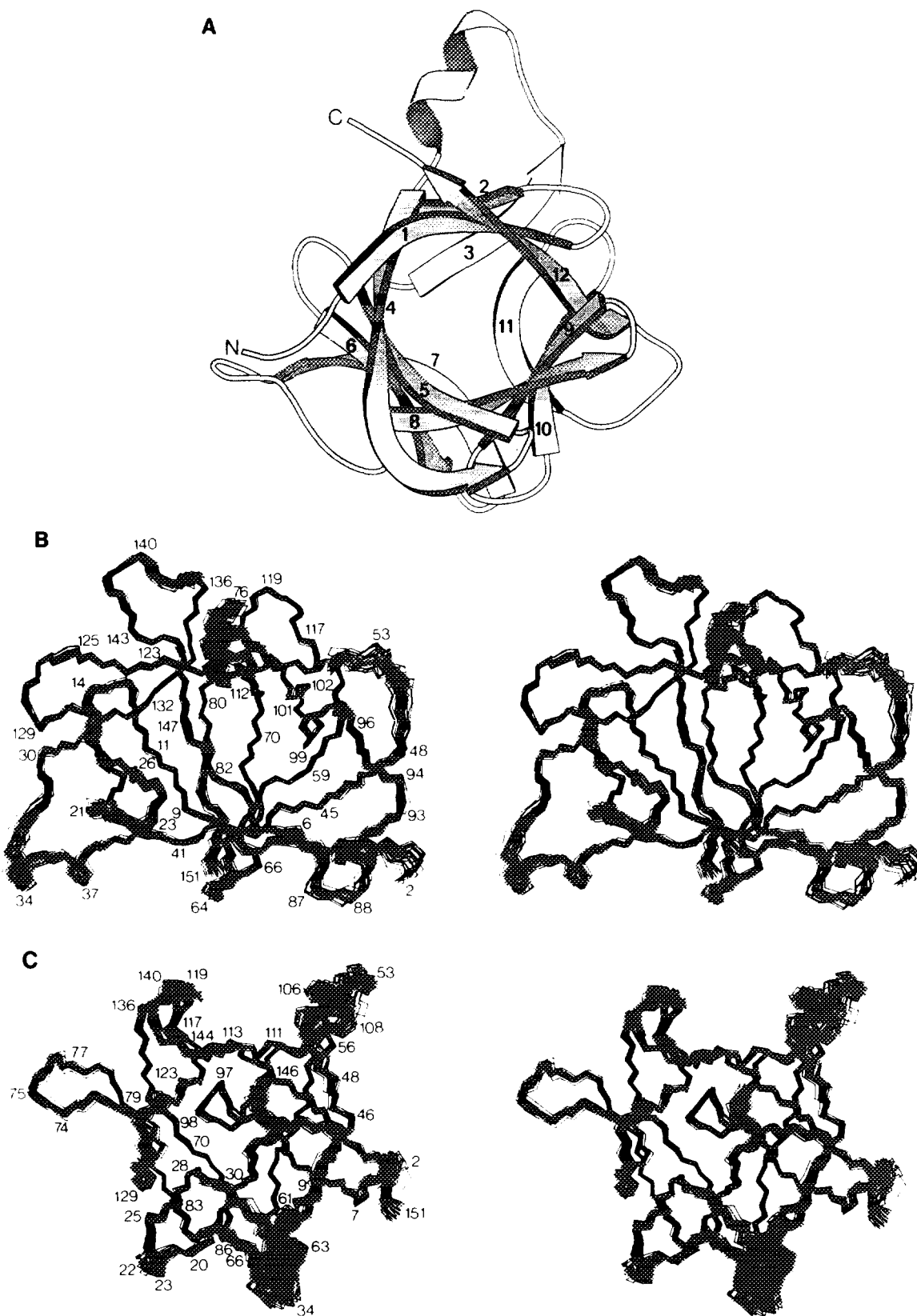
FIG. 1. (A) Schematic ribbon drawing of the solution structure of IL-1β with the open face of the β-barrel located in the front of the structure. (B, C) Two stereoviews showing superpositions of the backbone (N, C^{α}, C) atoms of the 32 calculated NMR structures. The average atomic rms distribution of the 32 structures about their mean coordinate positions is 0.41 ± 0.04 Å for the backbone atoms, 0.82 ± 0.04 Å for all atoms, and 0.49 ± 0.03 Å for all atoms of internal residues (i.e., side chains with a surface accessibility ≤40% of that in a Gly–X–Gly tripeptide). The ribbon drawing in (A) was generated with the program Molscript (69) and the strands are numbered 1 to 12. Adapted from Ref. 5.
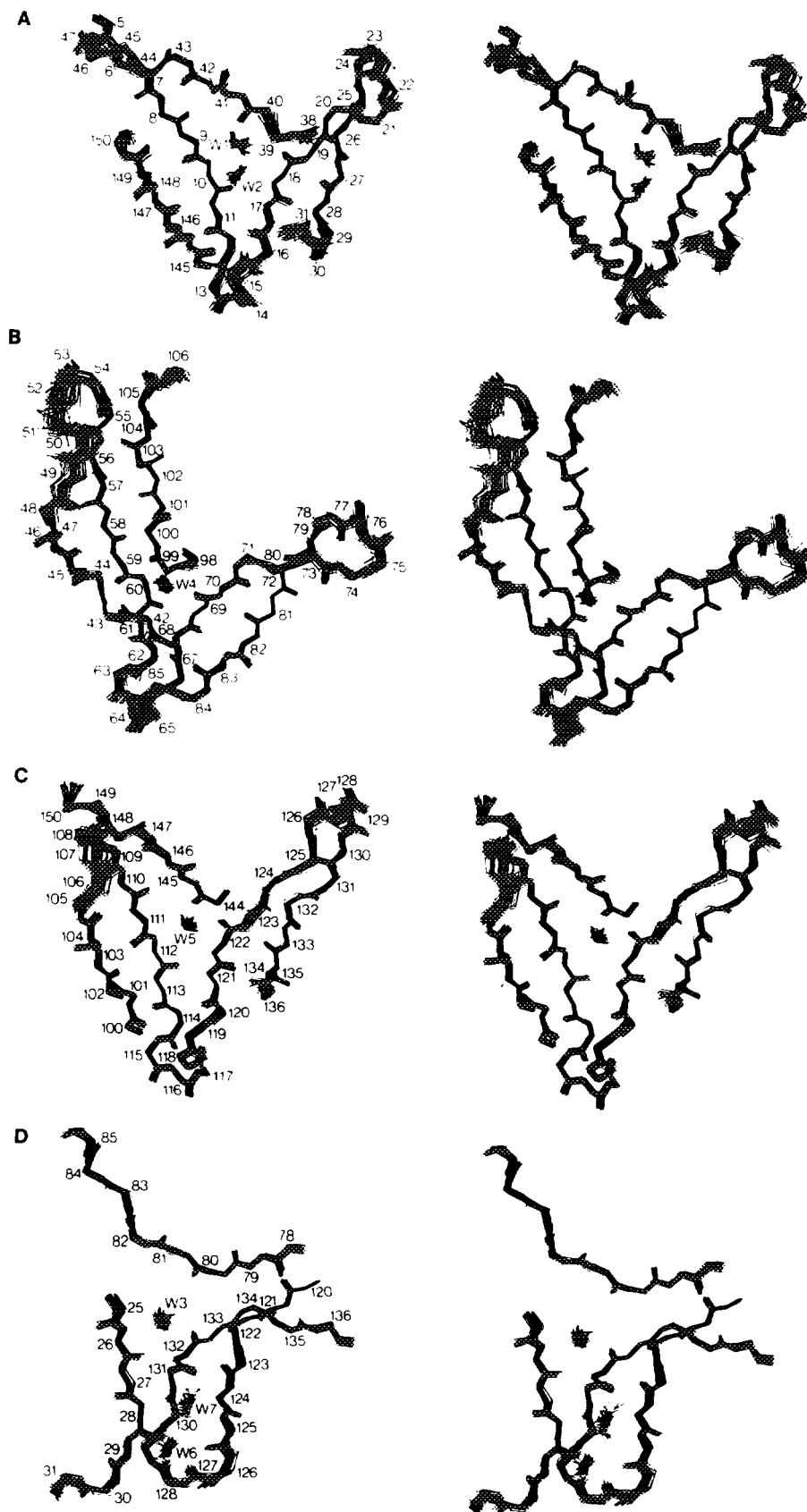
FIG. 2. Stereoviews showing superpositions of the backbone (N, C$^\alpha$, C, O) atoms and tightly bound structural water molecules of the 32 calculated NMR structures in the three repeating topological units of IL-1β (A-C) and the interface of the three units (D). Adapted from Ref. 5.

other six strands, as seen in the view shown in Fig. 1A. All the strands are regular with the exception of strand 4, which has a β-bulge.

Three pairs of strands are connected by classical four-residue β-turns: namely, strands 1 and 2 by a type I turn (residues 12–15) and strands 6 and 7 and strands 8 and 9 by type I' turns (residues 74–77 and 106–109, respectively). Another five pairs of strands are joined by irregular turns and/or short loops of 5–6 residues. These comprise the connections between strands 2 and 3 (residues 21–25), 4 and 5 (residues 51–55), 5 and 6 (residues 62–67), 10 and 11 (residues 125–130), and 11 and 12 (residues 136–141). Strands 3 and 4 are connected by an unusual 10-residue segment (residues 30–39) which comprises a type II turn (residues 32–35) followed by 2.3 turns of 3–10 helix (residues 33–39). The latter is characterized by 4 CO(i)–NH(i + 3) hydrogen bonds between residues 33 and 36, 34 and 37, 35 and 38, and 36 and 39. Finally, strands 7 and 8 are connected by a long 15-residue loop (residues 86–100) which contains two irregular type I turns (residues 86–89 and 97–100) and a type VIb turn (residues 89–92) with a cis-proline at position 90.

The locations of the seven tightly bound water molecules (W1 to W7) associated (i.e., ≤3Å) with the slowly exchanging backbone amide protons of Leu-10, Leu-18, Leu-26, Leu-60, Phe-112, Ser-125, Asn-129, and Met-130, all of which are not within hydrogen-bonding distance of any backbone or side-chain acceptor group, are shown in Fig. 2. In topological unit A W1 is involved in bridging hydrogen bonds between Leu-10 NH and Val-40 CO (in strand 4), while W2 participates in bridging hydrogen bonds between Leu-18 NH and Leu-10 CO (Fig. 2A). In topological unit B, the water molecule (W4) hydrogen bonded to Leu-60 NH donates two hydrogen bonds, one to the backbone carbonyl of Leu-69 in strand 6, the other to the backbone carbonyl of Phe-99 in strand 8 (Fig. 2B). In topological unit C, the bound water molecule (W5) displays exactly the same sort of hydrogen-bonding interactions as in topological unit B (Fig. 2C). In particular, W5 accepts a hydrogen bond from the NH of Phe-112 in strand 9 and donates two hydrogen bonds to the backbone carbonyls of Ile-122 in strand 10 and Thr-144 in strand 12. At the interface of the three units formed by strands 3, 7, and 9, the water molecule W3 bridges the NH of Leu-26 in strand 3 and the backbone carbonyl of Val-132 in strand 9 (Fig. 2D). Examination of Figs. 2A–2C clearly shows that these five bound water molecules occupy very similar spatial positions in the three topological units and at the interface of the three units, thereby playing an important role in stabilizing the structure. In addition to these five water molecules, there are two other bound waters involved in stabilizing the loop between strands 10 and 11 (Fig. 2D). In particular, W6 bridges a hydrogen bond between the NH of Ser-125 and the CO of Met-130 at the base of the loop, while W7 accepts hydrogen bonds from the NHs of Asn-129 and Met-130 and donates hy-

drogen bonds to the backbone carbonyls of Ala-127 and Ala-28. The latter interaction serves to stabilize the orientation of this loop with regard to strand 3.

The exterior of the protein is charged and hydrophilic, while the interior is highly hydrophobic. Nevertheless, of the 14 most buried residues (surface accessibility ≤3%, ≤5 Å^2), 7 are hydrophilic in nature, comprising two Cys (Cys-8 and -71), three Ser (Ser-70, -114, and -123), one Thr (Thr-124), and one Asp (Asp-12). The inaccessibility of the two Cys residues (which are not disulfide bridged and are separated by ~16 Å) accounts for their complete lack of reactivity toward sulfhydryl reagents in the native protein (9). In the main, the buried hydrophilic residues are involved in hydrogen bonding or electrostatic interactions. The carboxylate of Asp-12 (strand 1) participates in three hydrogen-bonding interactions with the backbone amides of Gln-14 and Lys-16 and the hydroxyl group of Thr-124. The first two hydrogen bonds serve to stabilize the turn between strands 1 and 2, while the third is important in positioning strands I and II relative to strands 10 and 11 (Fig. 1B). The SH group of Cys-71 (in strand 6) is hydrogen bonded to the hydroxyl group of Ser-114 (in strand 9), the hydroxyl group of Ser-70 (strand 6) is hydrogen bonded to the carboxylate side chain of Glu-83 in the adjacent strand (strand 7), and in strand 10 the hydroxyl group of Ser-123 is hydrogen bonded to the backbone carbonyl of Tyr-121.

The packing of some of the internal residues with respect to one another is illustrated in Fig. 3. Hydrophobic interactions are crucial in tethering the external strands, turns, and loops to the barrel. For example, residues 71–80, which comprise the end of strand 6 and the beginning of strand 7, together with the type I' turn between them, appear to be highly exposed to solvent (Fig. 1B), yet their orientation with respect to the core of the protein is stabilized by numerous interactions involving strands 7, 9, 10, and 11, as well as the loop connecting strand 9 and 10 (Fig. 3A). Thus, the buried Cys-71 is in close proximity to Leu-134 in strand 11; Leu-73 and Pro-78 interact with Phe-117, which is located in the loop between strands 9 and 10; and Leu-80 is close to Ile-122 in strand 10. Furthermore, Pro-78 is sandwiched between Phe-117 and Trp-120 (Fig. 3A), which is also important in fixing the position of the connecting loop between strands 10 and 11 (residues 115–120). In addition, the position of the exposed turn comprising residues 74–77 is stabilized by an electrostatic interaction between the N$^\zeta$H$_3^+$ of Lys-74 and the amino group of Gln-81 in strand VII. Another highly exposed loop is that between strands 11 and 12 (residues 136–141; Fig. 1B). In this case Trp-120 in strand 10 is closely packed against Gly-135 and -136, and there is a salt bridge between Lys-138 and Glu-111 (strand 9). In addition, the beginning of strand 12 is tethered by hydrophobic interactions between Ile-143, Ser-13 (strand 1), and Thr-124 (strand 10) and between Thr-144 and

Tyr-121 (strand 10) and by an electrostatic interaction between the side chains of Asp-145 and Ser-13.

A similar dense network of interactions is found for the other loops. For example, the connecting segment between strands 3 and 4 (residues 30–39) is stabilized by hydrophobic interactions between Leu-31 and residues in strands 2 (Val-19) and 3 (Leu-29), and the 3–10 helix (residues 33–39) is further stabilized by an electrostatic interaction between the side-chain carboxylate of Asp-35 and the amino group of Gln-38. The short loop (residues 51–56) between strands 4 and 5 is stabilized by hydrophobic interactions with residues on strand 8, namely,
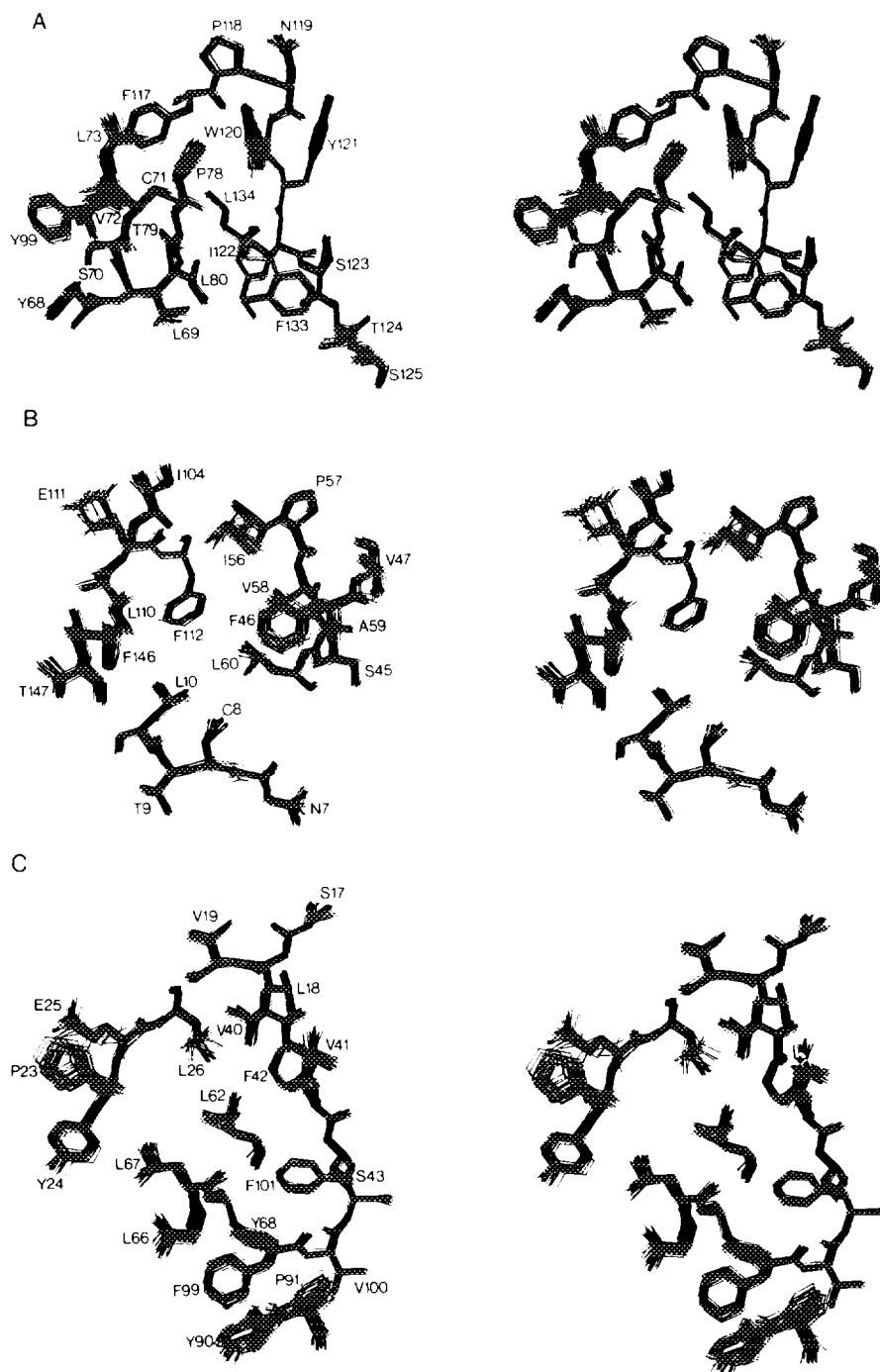

FIG. 3. Stereoviews showing superpositions of all atoms (excluding protons) of the 32 calculated NMR structures for three selected segments of IL-1β. Adapted from Ref. 5.

between the aliphatic portion of the side chain of Lys-53 and Ile-104 and between Ile-56 and the aliphatic portion of the side chain of Lys-103. The short loop between strands 5 and 6 (residues 62–67) is stabilized by hydrophobic interactions between Leu-62, Leu-67, and residues in strand 3 (Tyr-24, Leu-26), 4 (Val-40 and Phe-42), and 7 (Leu-80 (Figs. 3A and 3C).

In the case of the long loop between strands 7 and 8 (residues 86–100), Val-85, Tyr-90, and Phe-99 are close to Tyr-68 in strand 6 (Figs. 4A and 4C), Met-95 is close to hydrophobic residues in strands 4 (Val-47) and 5 (Ala-59), there is a potential electrostatic interaction between the side chain of Asn-66 (strand 6) and the backbone nitrogen atom of Pro-87, and finally there is a backbone hydrogen bond between the NH of Gln-48 (strand 4) and the carbonyl oxygen of Lys-93. In addition, some of the local features, such as the two type I turns, are stabilized by short-range electrostatic interactions, in particular between the side chains of Asp-86 and Asn-89 and between Glu-96 and Arg-98.

The short loop between strands 10 and 11 (residues 125–130) displays two side-chain–side-chain electrostatic interactions with residues on strand 3, namely, between Glu-128 and His-30 and between Asn-129 and Lys-27. In this regard it is interesting to note that although His-30 is exposed to solvent (cf. Fig. 2A) it displays a high pK_a of 7.5 (10), which can be attributed to its interaction with the negatively charged carboxylate of Glu-128.

Comparison of Solution and X-Ray Structures

The solution and X-ray structures are very similar both locally and globally, as shown by the best fit superposition in Fig. 4. The rms difference between the solution NMR structure and three independently solved X-ray structures is ~0.9 Å for the backbone atoms and ~1 Å for all atoms of internal residues, with the largest differences being

confined to some of the loops and turns connecting the β-strands. These can sometimes involve rigid body displacements, as is the case for the loops connecting β-strands 3 and 4 (residues 32–39) and 7 and 8 (residues 84–91) and for the turn connecting β-strands 8 and 9 (residues 106–109). Such differences are mainly due to crystal packing forces. Of particular interest is that the atomic rms distribution of the calculated solution structures about their mean coordinate positions (~0.4 Å for backbone atoms, ~0.8 Å for all atoms, and ~0.5 Å for all atoms of internal residues) is approximately the same as the atomic rms differences between the three X-ray structures, indicating that the positional errors in the atomic coordinates determined by the two methods are similar (11).

Joint Refinement Using Combined NMR and X-Ray Data

Upon initial inspection, the X-ray structures appear to be incompatible with the NMR data, as manifested by a relatively large number of NOE and torsion-angle violations. Conversely, the NMR structures fit the X-ray data poorly, with an R factor of 40–50%. Because of the very different nature of the two methods, it is not immediately apparent that these discrepancies reflect genuine differences between the solution and X-ray structures or whether they reflect differences in the computational procedures employed. To resolve this question, we demonstrated (12) that a model can readily be generated from a joint X-ray/NMR refinement which is compatible with the data from both techniques. Thus, there are only minimal violations of the NMR restraints (NOEs and torsion angles), the value of the crystallographic R factor is comparable to, if not slightly better than, that derived from refinement against the crystallographic data alone, and the deviations from idealized covalent geometry are small.
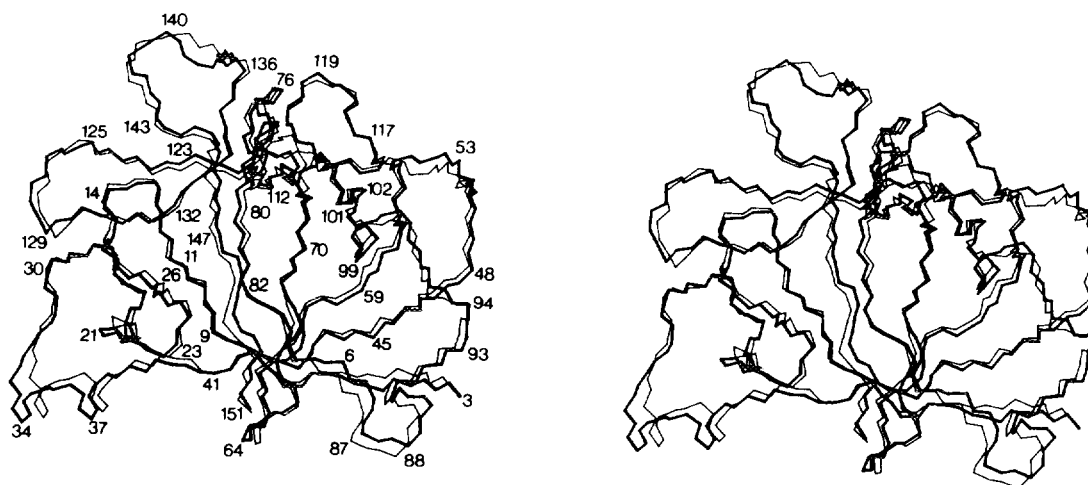

FIG. 4. Stereoview of a best-fit superposition of the backbone (N, C^α, C) atoms of the restrained minimized mean NMR structure (thick lines) and the X-ray structure (thin lines) of IL-1β. The X-ray structure is from Ref. 6. Adapted from Ref. 9.

In addition, the free R factor for the model refined with the combined NMR and X-ray restraints is actually smaller than that of the model obtained by conventional crystallographic refinement, indicating that the crystallographic phases obtained by the joint refinement method are more accurate. The few observations that are still violated serve as an indicator for genuine differences between the crystal and the solution structures. These are principally located in the loops connecting β-strands 3 and 4 and β-strands 7 and 8. In the crystal, these two loops are involved in intermolecular contacts with each other between neighboring molecules in the lattice.

Folding of Interleukin-1β

The kinetics of folding of IL-1β have been studied by NMR, circular dichroism (CD), and fluorescence (13). Ninety percent of the β-structure content present in the native protein, as monitored by far-ultraviolet (UV) CD, is attained within 25 ms, correlating with the first kinetic phase determined by tryptophan and 1-anilinonaphthalene-8-sulfonate (ANS) fluorescence. In contrast, stable native secondary structure, as measured by quenched-flow deuterium/hydrogen (D/H) exchange experiments, starts to be formed after only 1 s, and the NMR experiments indicate the formation of at least two intermediates with half-lives of 0.7–1.5 and 15–25 s, with the final stabilization of secondary structure occurring on a time scale much greater than 25 s. These results are summarized in Fig. 5. The rapid acquisition of far-UV CD ellipticity can therefore be ascribed only to the formation of unstable β-like secondary structure. In other words, any hydrogen bonds that are formed early in the folding pathway are not stable due to either local breathing or sliding of one strand relative to another, resulting in the rapid formation and breaking of hydrogen bonds. The formation of the first NMR intermediate correlates with the third phase in the ANS kinetics, which are associated with a substantial increase in ANS fluorescence. Most of topological unit B and part of topological unit C are formed at this stage, but large clusters of hydrophobic residues are still available for ANS binding. The second intermediate is formed at a somewhat lower rate than the second phase in the far-UV CD kinetics (half-life ~6 s) and involves the completion of topological units B and C. During this time frame, desorption of ANS begins to occur, implying that hydrophobic residues are being buried within the protein core. The complete formation of stable secondary structure, which is principally associated with the formation of topological unit A, occurs on a time scale similar to that of the late-phase packing of Trp-120 into its native environment and the final desorption of ANS (half-life ~20 min).

From these data, it is apparent that the folding of an all-β-sheet protein such as IL-1β proceeds in a manner substantially different from that of mixed α-helix/β-sheet proteins in which both α helices and β sheets are stabilized
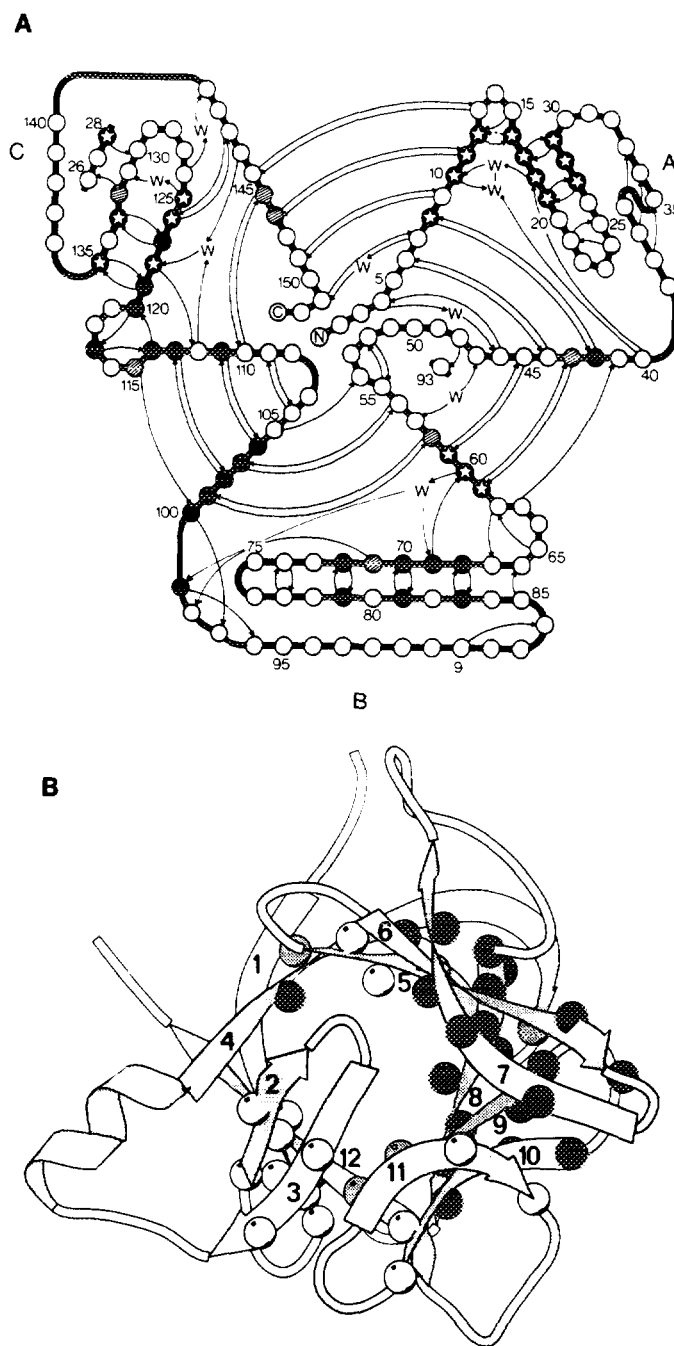

FIG. 5. Summary of the refolding of IL-1β as observed in the quenched flow D/H amide protection experiments. (A) Schematic diagram of the hydrogen bonding and topology of IL-1β. The positions of amide groups that are protected during folding with a $t_{1/2}$ of 0.7–1.5, 15–25, and $\geqslant$25 s are indicated by black circles, hatched circles, and black circles with a white star, respectively. (B) Ribbon diagram of the polypeptide fold of IL-1β illustrating the spatial location of the amide groups protected during folding. The residues of amide groups protected with a $t_{1/2}$ of 0.7–1.5, 15–25, and $\geqslant$25 s are shown as black, gray, and white circles, respectively. In the view shown, the open face of the β-barrel is located in the back of the structure. The ribbon drawing was generated using the program Molscript (69). Adapted from Ref. 13.

very rapidly (less than 10–20 ms). In all these cases, the regions of native β-sheet that are detected first are those involved in tertiary interactions with a helix or helices that are also stably formed early in the folding process (due to the fact that the hydrogen-bonding interactions involved in helix formation are local, extending over at most four residues for one turn of helix). In the native structure of the all-β protein IL-1β, on the other hand, the three pseudo-symmetric elements of β-sheet do not form such interactions. Each β-strand contributes two or three nonpolar residues to a hydrophobic core that depends for its stability on the hydrophobic and van der Waals interactions of a large number of tightly packed side chains. This suggests that folding to the stable native structure for this type of protein involves the rapid formation of β-structure around a nonpolar core, followed by the much slower stabilization of native secondary structure that accompanies the progressive final tight packing of the core groups and/or those groups external to the β-sheets.

Relationship of Structure to Function

With the structure of IL-1β in hand, it is now possible to interpret the results of chemical modification and mutagenesis studies in structural terms (5).

Several lines of evidence indicate that the large concave face of the molecule formed by residues 19–27 (strands 2 to 3), 70–84 (strands 6 and 7), and 121–142 (strand 10 to the beginning of strand 12) is not involved in receptor binding. This face is located at the "back" of the molecule on the side opposite to the front end of the β-barrel (i.e., at the back of Figs. 1A and 1B and at the front of Fig. 4B). First, mutations of Tyr-24 → Phe, Lys-27 → Cys, Trp-120/Tyr-121 → Phe/Phe, and Lys-138 → Cys have no effect on receptor binding (14, 15). Second, derivatization of the Lys-77 → Cys mutant with an ∼60,000-kDa biotin–streptavidin complex through the surface-accessible SH group has no effect on receptor binding (P. T. Wingfield, personal communication). Similarly, derivatization of the Lys-138 → Cys mutant with phycobiliprotein, a protein of 240,000 kDa, does not affect receptor binding (15).

Mutants that influence either receptor binding and/or activity are located in three distinct regions of the molecule. The first region comprises the N- and C-termini, which are located close together in space (Figs. 1A and 1B). While removal of the N-terminal residues up to but excluding Arg-4 has little effect on receptor binding (16), mutation of Arg-4 to either Glu (17) or Asp (16) reduces both receptor binding and activity almost 1000-fold. The importance of the N-terminus is further highlighted by two additional pieces of evidence. First, receptor binding of the unprocessed N-terminal methionylated IL-1β is 10-fold lower than that of the mature protein (18), and second, derivatization of a mutant in which a cysteine was inserted between Ala-1 and Pro-2 with streptavidin

leads to the complete abolition of receptor binding (5). Similarly, deletion of more than the last three residues at the C-terminus severely reduces receptor binding (16, 19). Examination of the surface of the protein reveals a potential binding cleft (located on the right-hand side of Figs. 1A and 1B) with a radius of ∼8 Å comprising the following surface-accessible residues (5): Arg-4 and Leu-6 from strand 1, Phe-46 from strand 4, Ile-56 from strand 5, Lys-103 and Glu-105 from strand 8, Asn-108 and Leu-110 from strand 9, and Met-148 and Phe-150 from strand 12. This suggestion based on the structure (5) was subsequently confirmed in its entirety by more extensive mutagenesis studies (20).

The second region (5) is characterized by mutations of Arg-11 and His-30. The Arg-11 → Gly mutant displays a very small (∼25%) reduction in receptor binding but a 100-fold reduction in biological activity (21). The His-30 → Asn and His-30 → Arg mutants exhibit 30- and 100-fold reductions, respectively, in receptor binding (14). Both residues are located in a possible second binding cleft on the molecule located at the lower left-hand side of Figs. 1A and 1B. This site has a radius of ∼7 Å and comprises Arg-11 and Gln-15 from strand 1; His-30, Gln-32, Met-36, and Gln-39 from the segment connecting strands 3 and 4 (which comprises the 3–10 helix from residues 33–39); and Gln-149 from strand 12 at the C-terminus. A ridge-like border between this site and the first one is formed by strand 12. It is also interesting to note that the decrease in receptor binding affinity produced by the presence of both the N-terminal Met and the His-30 → Arg mutation is additive rather than synergistic (18), providing further evidence that sites 1 and 2 constitute two distinct receptor binding sites (5).

The third site (5) is defined by the mutation of Asp-145 → Lys, which has minimal effects on receptor binding but reduces biological activity significantly (22). This cleft has a radius of 5–6 Å and is located at the top left of Figs. 1A and 1B and at the top middle of Fig. 1C. It is formed by Ser-13 and Gln-14 of strand 1, Lys-109 of strand 9, Gln-126 of strand 10, and Asp-145 of strand 12. The border between the third and the first binding sites is formed by the turn (residues 105–108) between strands 8 and 9, while the border with the second site is formed by the turn (residues 12–15) between strands 1 and 2.

These three regions occupy a large surface area of the protein. For example, the distances between His-30 and Arg-4, Asp-145 and Arg-4, and His-30 and Asp-145 are ∼33, ∼26, and ∼14 Å, respectively. Interestingly, the amino acid sequence of the extracellular ligand binding portion of the IL-1β receptor reveals three immunoglobulin-like domains, all of which may be required for receptor binding and/or biological activity (23). This suggests that each domain of the receptor may bind to one of the three postulated receptor binding sites on IL-1β, and, in light of the mutational data, leads one to speculate that the first site contributes most of the binding energy,

while the second and third sites may play a role in signal transduction, internalization of the IL-1β/IL-1 receptor complex, and cellular and nuclear targeting (5).

INTERLEUKIN-4

IL-4 is a protein of $\sim$15 kDa that regulates B-cell proliferation and differentiation, modulates the survival, proliferation, and differentiation of T cells, acts as a growth factor on mast cells, regulates macrophage activation, and induces the expression of VCAM-1 on endothelial cells (24–28). IL-4 is a potent inducer of human cytotoxic CD8$^+$ T cells, an activity that has been shown to be responsible for establishing tumor-specific systemic immunity to an established renal cancer by injection of renal tumor cells genetically engineered to secrete large doses of IL-4 locally (29). The very potent antitumor activity of IL-4 at the primary tumor site is also associated with the elicitation of a localized inflammatory infiltrate, dominated by eosinophils (30, 31). Additionally, IL-4 induces the expression of Class I and II MHC molecules and the IgE low-affinity receptor on resting B cells. IL-4 causes immunoglobulin class switching of activated B cells to IgE and IgG1, thereby generating and sustaining *in vivo* IgE responses and ensuring the dominance of IgG1 in a T-cell-dependent immune response (32).

The solution structure of IL-4 has been solved independently by two groups at low/medium resolution (33, 34). More recently, a high-resolution solution structure has been determined using three- and four-dimensional heteronuclear NMR spectroscopy on the basis of 2973 experimental NMR restraints (35). Following the solution structure determination, two X-ray structures at $\sim$2.3 Å resolution were published (36, 37).

The Solution Structure of IL-4

The overall structure of IL-4[1] consists of four α-helices arranged in a left-handed helical bundle (Fig. 6). A unique characteristic of the IL-4 structure is the orientation of the helices in which adjacent helices are antiparallel while nonadjacent opposing helices are parallel. This results in

[1] The numbering scheme for human recombinant IL-4 used in this paper includes the four-residue sequence Glu-Ala-Glu-Ala at the N-terminus of the recombinant protein which is not part of the natural human IL-4; the natural sequence therefore starts at residue 5, and 4 should be subtracted from the residue number to get the number of natural IL-4.

two overhand connections in the form of two long loops with some irregular β-strand characteristics. Indeed, parts of these two long loops actually form a short antiparallel β-sheet between residues 32–34 and 110–112. Helix α_A (residues 8–24) leads into a five-residue helical turn (ht$_A$, residues 27–31) followed by a strand (β_A, residues 32–34) that runs in a direction antiparallel to helix α_A and a loop (residues 35–43) that leads into helix α_B (residue 44–66). Helices α_B and α_C (residues 73–98) are connected by a short loop (residues 67–72) that contains a five-residue helical turn (ht$_B$, residues 67–71). Helix α_C leads into a loop (residues 99–109) and a short strand (β_B, residues 110–112) that runs antiparallel to α_C and leads directly into the fourth helix α_D (residues 113–128).

The structure of IL-4 contains three disulfide linkages (Fig. 6). The N- and C-termini of the protein are connected by the disulfide bond between Cys-7 and Cys-131, which is ill-defined. The disulfide bridge between Cys-28 and Cys-69 connects the two helical turns, ht$_A$ and ht$_B$, while that between Cys-50 and Cys-103 connects helix α_B to the loop from residues 99 to 109.

The IL-4 molecule is oblong in shape with approximate dimensions of 41 $\times$ 28 $\times$ 19 Å. This is reflective of the four relatively long α-helices of approximately equal length that are packed into the left-handed bundle. The angles and axial separations between the long axes of the four antiparallel helical pairs, α_A–α_C, α_C–α_B, α_B–α_D, and α_D–α_A, are $-157°$ and 11.1 Å, $-154°$ and 10.2 Å, $-152°$ and 7.7 Å, and $-148°$ and 11.8 Å, respectively. The corresponding values between the parallel helical pairs, α_A–α_B and α_C–α_D, are 40° and 14.9 Å and 36° and 15.1 Å, respectively.

The nature of the helix packing is dependent on side-chain–side-chain interactions (Fig. 7). The core of the IL-4 protein is entirely hydrophobic. The residues involved in the helix packing are Leu-11, Ile-14, Leu-18, and Leu-21 of helix α_A; Phe-49, Ala-52, Ala-53, Leu-56, Phe-59, and Tyr-60 of helix α_B; Leu-83, Ile-84, Leu-87, Leu-90, Leu-94, and Leu-97 of helix α_C; and Leu-113, Phe-116, Leu-117, Leu-120, Met-124, and Tyr-128 of helix α_D. In addition, there are a number of hydrophobic interactions between strand β_A and helices α_B and α_D. Specifically, Val-33 of strand β_A is in contact with Val-55 and Phe-116, Ile-36 is in contact with Ala-52, and Phe-37 is in contact with Ile-123.

It appears from Fig. 6 that residues 73–80 in helix α_C extend beyond the helix bundle and are solvent exposed. The orientation of this segment of helix α_C with respect to the core of the protein, however, is well defined and is

---

FIG. 6. (A) Schematic ribbon drawing of the solution structure of recombinant human IL-4. (B, C) Two stereoviews showing superpositions of the backbone (N, C$^\alpha$, C) atoms of the 30 calculated NMR structures. The average atomic rms distribution of the 30 structures about their mean coordinate positions for residues 8–129 is 0.44 $\pm$ 0.03 Å for the backbone atoms, 0.83 $\pm$ 0.03 Å for all atoms, and 0.51 $\pm$ 0.04 Å for all atoms excluding disordered side chains. The N-terminal (residues 1–7) and C-terminal (residues 130–133) residues are disordered. Note that the natural IL-4 sequence starts at residue 5. The ribbon drawing in (A) was generated with the program Molscript (69). Adapted from Ref. 35.

A

B

C
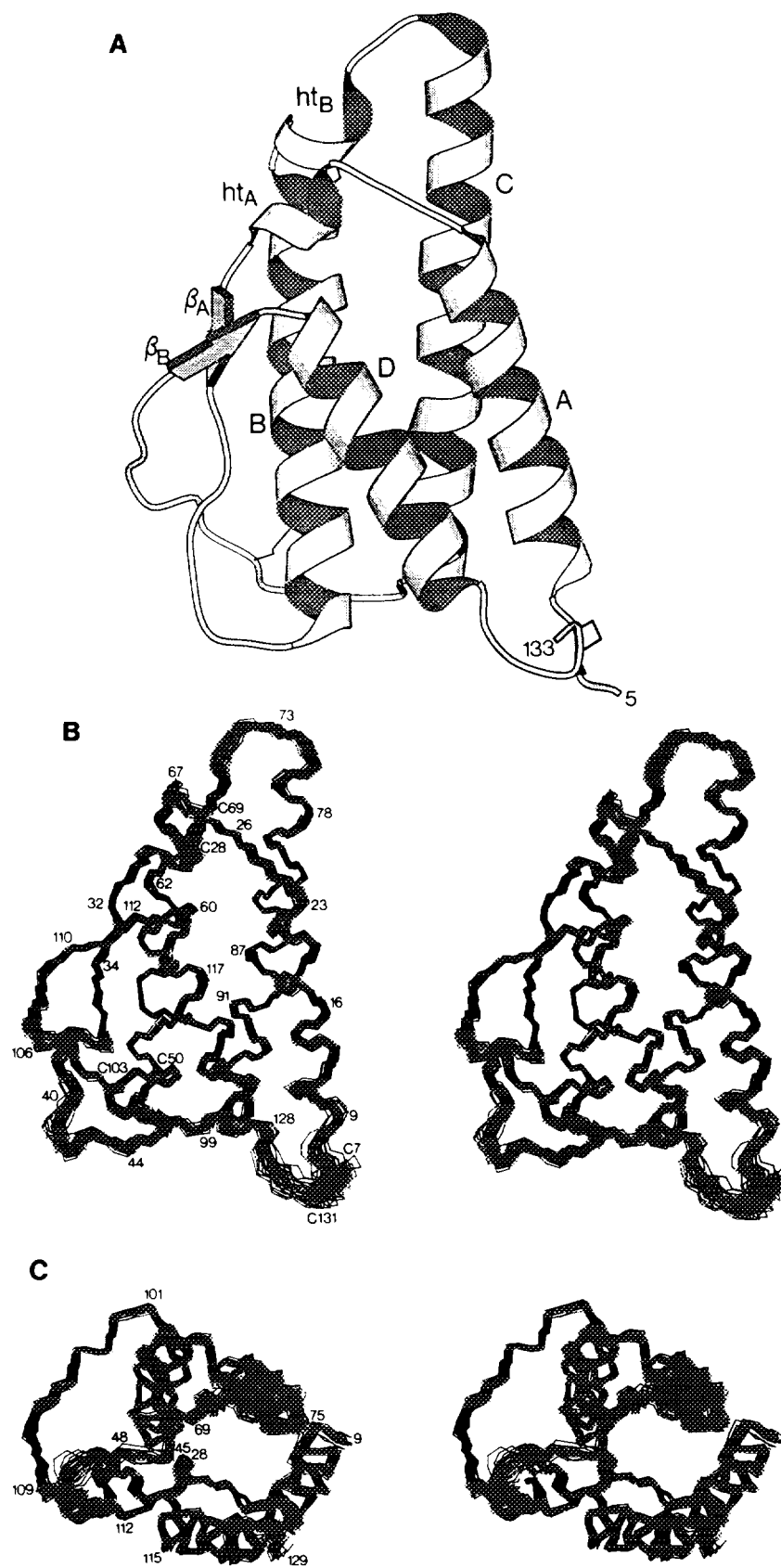
stabilized by numerous hydrophobic side-chain–side-chain interactions involving the helical turns ht_A and ht_B. In particular, Gln-76 is in close proximity to Thr-26 and Leu-27, Phe-77 is in close proximity to Leu-70, Arg-79 is in close proximity to Gln-24 and Thr-26, and His-80 is in close proximity to His-63, Glu-64, Cys-69, and Leu-70 (Fig. 7C).

While the interior of IL-4 is highly hydrophobic, the exterior is highly hydrophilic and comprises a high percentage of charged residues (12 Lys, 9 Arg, 8 Glu, and 6 Asp). Analysis of the structure suggests the presence of eight *potential* hydrogen bonds or salt bridges involving surface side chains (Fig. 8).

Some of the hydrogen bond/salt bridge interactions involve neighboring residues in a helix or helical turn, thereby contributing further to its stability. Examples of this type of interaction include the hydrogen bonds between the hydroxyl group of Thr-29 and the backbone carbonyl of Thr-26 in helical turn ht_A, between the hydroxyl group of Thr-48 and the backbone carbonyl of Thr-44 in helix α_B, and between the hydroxyl group of Thr-112 and the side-chain amide group of Asn-115 in helix α_D. The remaining interactions are clearly involved in stabilizing the packing of the four helices and/or maintaining the tertiary structure of IL-4. Specifically, there are three interhelical interactions: the carbonyl side chain of Asn-19 in helix α_A is hydrogen bonded to the $N^\zeta H_3^+$ group of Lys-121 in helix α_D; the carboxylate side chain of Glu-45 at the N-terminus of helix α_B is salt bridged to the $N^\zeta H_3^+$ of Lys-127 at the C-terminus in helix α_D; and the side-chain amide group of Gln-58 in helix α_B is hydrogen bonded to the hydroxyl group of Thr-24 in helix α_A. Finally, there are two interactions that stabilize the positioning of strand β_A with respect to helices α_B and α_D: namely, the carboxylate side chain of Asp-35 at the end of strand β_A is hydrogen bonded to the guanidinium group of Arg-119 in helix α_D, and the backbone carbonyl of Ala-39 in the loop connecting helix α_B and strand β_A is hydrogen bonded to the guanidinium group of Arg-51 in helix α_B. The hydrogen bond/salt bridge involving Asp-35 is of particular interest as it serves to neutralize the negative charge on the completely buried side chain of Asp-35, which has a surface accessibility of only ~6 $Å^2$.

Comparison of the Solution Structure of IL-4 with the X-Ray Structure

The superposition of the backbone atoms of the high-resolution NMR structure and the 2.25-Å-resolution X-ray structure of Wlodawer *et al.* (36) is shown in Fig. 9. Clearly, the two structures are similar, in terms of both overall topology and alignment of the four helix bundle. Nevertheless, there are some significant differences, as evidenced by the relatively large rms differences between the two structures. Thus, excluding residues 1–7 and 130–133 at the N- and C-termini, respectively, the atomic rms difference between the restrained minimized mean NMR

structure and the X-ray structure is 1.37 Å for the backbone atoms and 2.24 Å for all atoms. When only residues involved in secondary structure are considered, these values drop to 1.04 and 1.94 Å, respectively.

These relatively large rms differences can be attributed to rigid body displacements of the helices such that the four-helix bundle is more tightly packed in the crystal structure than the NMR structure. In particular, the axial separation for three pairs of helices, α_A–α_C, α_A–α_D, and α_C–α_D, is reduced by approximately 20% from 11.1, 10.2, and 15.1 Å, respectively, in the NMR structure to 8.8, 8.5, and 12.3 Å, respectively, in the crystal structure. This is also accompanied by a decrease in the radius of gyration from 14.7 Å in the NMR structure to 14.2 Å in the crystal structure. The higher degree of compactness of the crystal structure can probably be attributed to mobility and flexibility of the protein in solution and to crystal packing forces arising from interactions with neighboring protein molecules in the crystal lattice. In this regard it is interesting to note that in the crystal lattice residues 66–76 in the loop connecting helices α_B and α_C are in contact with the N-terminus of helix α_A and the C-terminus of helix α_C of a second molecule and with the C-terminus of helix α_D of a third molecule.

The other major differences between the NMR and crystal structures lie in three loop regions comprising residues 35–43, 67–72, and 99–109, which connect helices α_A and α_B, helices α_B and α_C, and helices α_C and α_D, respectively. Again, mobility in solution and crystal packing are likely to be major contributors to these differences. Thus, for example, residues 40–45 of one molecule lie antiparallel to residues 40–45 of a second molecule in the crystal lattice, with four hydrogen bonds between the two molecules at this location [Ser-40 (CO)–Thr-48′ ($O^{\gamma 1}H$), Thr-43 (NH)–Asn-42′ (O^δ), Thr-44 (NH)–Lys-41′ (CO), and Thr-44 (NH)–Ser-40′ (CO)]. Similarly, the orientation with respect to the core of the protein of the loop comprising residues 67–72 is clearly influenced by crystal packing as described above. In solution, on the other hand, ^{15}N heteronuclear relaxation measurements indicate that the loops comprising residues 35–43 and 99–109 exhibit a significant degree of motion on the picosecond time scale and are characterized by low (0.2–0.6) values for the overall order parameters S^2 (38).

Comparison of the Solution Structure of IL-4 with the Crystal Structures of Human Growth Hormone and Granulocyte–Macrophage Colony-Stimulating Factor

The left-handed four-helix-bundle motif with two overhand connections observed in the structure of IL-4 is relatively unique. This topology has been observed in only four other proteins, all of which bind to the same superfamily of hematopoietic receptors (28): namely, growth hormone (39, 40), granulocyte–macrophage colony-stimulating factor (GM-CSF) (41, 42), interleukin-2 (43, 44), and macrophage colony-stimulating factor (45).

Even though there is no significant overall sequence identity between IL-4, human growth hormone (HGH), and GM-CSF, their overall topology is very similar, as illustrated both by the ribbon diagrams shown in Fig. 10 and by the observation of very similar values for the interhelical angles and axial separation within the four-helix bundle. There is one significant topological difference, however, between IL-4 and GM-CSF on the one hand
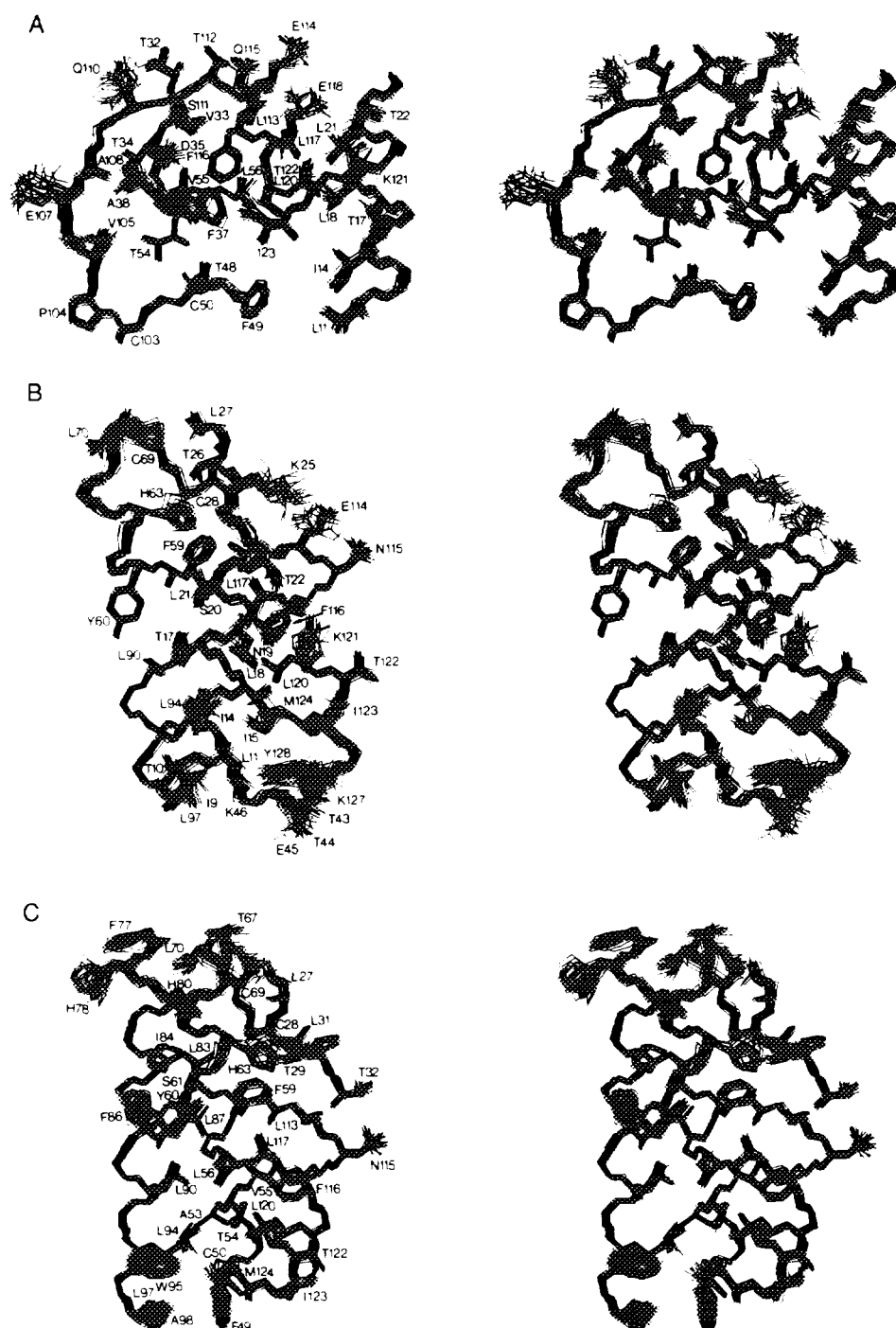

FIG. 7. Stereoviews showing best-fit superpositions of all atoms (excluding hydrogens and backbone carbonyls) of the 30 calculated NMR structures for three selected segments of recombinant human IL-4. Side-chain–side-chain interactions between helices α_A, α_B, and α_D and β-strands β_A and β_B are shown in (A), between helices α_A, α_C, and α_D in (B), and between helices α_B, α_C, and α_D in (C). Note that the natural IL-4 sequence starts at residue 5. From Ref. 35.

and HGH on the other. Namely, in the case of IL-4 and GM-CSF the N-terminal end of the overhand loop connecting helices α_A and α_B passes behind helix α_D in the view shown in Fig. 12, while in the case of HGH it passes in front of helix α_D.

A least-squares match of the C^α coordinates reveals that 72 residues of IL-4 and GM-CSF and 79 residues of IL-4 and HGH can be superimposed with an atomic rms difference of 1.7 and 2 Å, respectively. The resulting best-fit superpositions are also shown in Fig. 10, and the corresponding sequence alignments are given in Fig. 11. The extent of sequence identity within these matched regions of structure is small: 25% for IL-4 and GM-CSF and only 10% for IL-4 and HGH.

The principal differences between IL-4, GM-CSF, and HGH reside in the relative lengths of the helices, the nature and length of connecting elements, and the number and pattern of disulfide bonds. Inspection of the ribbon drawings shown in Fig. 10 indicates that GM-CSF is smaller than IL-4, whereas HGH is larger than IL-4. This is reflected in the lengths of all helices in the three structures. The helices in GM-CSF, IL-4, and HGH range from 10 to 20, 17 to 26, and 21 to 33 residues, respectively, in length. In addition, the relative lengths of the helices in each structure differ. In the case of HGH, helices α_A and α_D are longer than helices α_B and α_C, whereas the reverse is true for IL-4. For GM-CSF, helices α_A and α_C are longer than α_B and α_D. These differences result in a distinct alteration in the surface at the top of the front face in the view shown in Fig. 10.

The connecting elements between the various helices also differ in the three structures. IL-4 has two helical turns, one connecting helices α_A and α_B and the other connecting helices α_B and α_C, and a small antiparallel β-sheet connecting the two loops between helices α_A and α_B and helices α_C and α_D. In GM-CSF, the helical turn between helices α_B and α_C is missing. This is probably due to the fact that this connecting element is significantly shorter in GM-CSF (3 residues) than in IL-4 (6 residues). Conversely, the antiparallel β-sheet is 2 residues longer in GM-CSF than in IL-4. The differences in the connecting elements between IL-4 and HGH are more distinctive. In HGH, the antiparallel β-sheet is absent and an additional short (7-residue) helix is present between helices α_A and α_B. This additional helix can be formed because the linker between helices α_A and α_B is approximately twice as long as the linker in IL-4 (37 residues compared to 19 residues) and, hence, does not need to adopt an entirely extended conformation to complete the link between the two helices.

In addition, the pattern and number of disulfide linkages differ in the three structures. IL-4 has three disulfide bridges, whereas both HGH and GM-CSF have only two disulfide linkages. The disulfide linkages in GM-CSF connect helix α_B to the loop region between helices α_C and α_D and the C-terminus to helix α_C. The disulfide linkages in HGH connect helix α_D to the loop region between helices α_A and α_B and the C-terminus to helix α_D.

Biological Implications

The striking qualitative and quantitative resemblance of the topologies of IL-4, GM-CSF, and HGH illustrated in Fig. 10 was unexpected given the very limited amount of overall sequence similarity. One rationale for this ob-
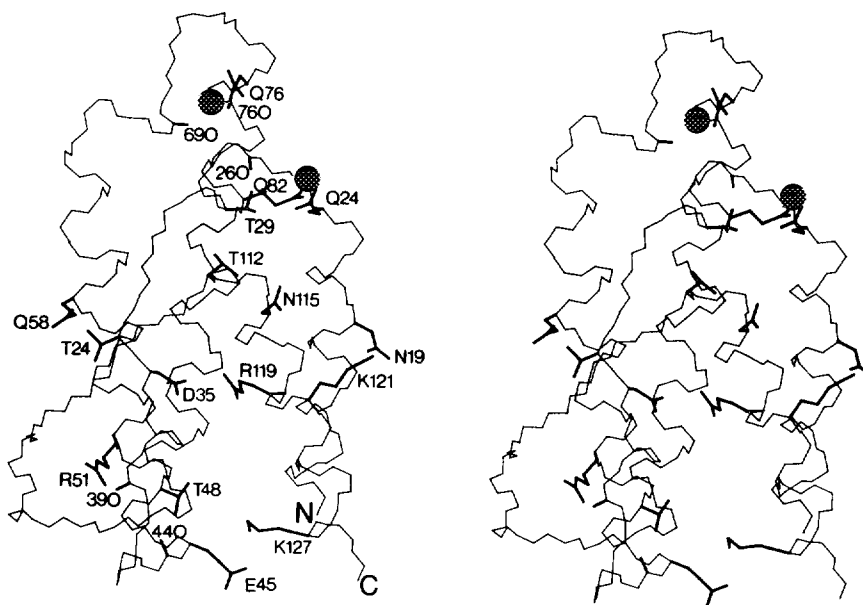

FIG. 8. Stereoview of the backbone (N, C^α, C) atoms of the restrained minimized mean NMR structure of human recombinant IL-4 (residues 9–129), together with the side chains or backbone carbonyl groups of residues involved in hydrogen bonds and salt bridges. The locations of two tightly bound water molecules are indicated by the filled-in circles. Note that the natural IL-4 sequence starts at residue 5. From Ref. 35.

servation may be provided by the fact that the receptors for these three proteins belong to the same hematopoietic superfamily. If this interpretation is accurate, then one would expect all three proteins to interact with their cell surface receptor in a similar manner. The crystal structure of the HGH–receptor complex has been determined (38) and reveals that a single molecule of HGH is bound to two molecules of receptor. This has lent support to the hypothesis that dimerization is responsible for signal transduction by the hematopoietic superfamily of receptors (28, 46, 47). It may therefore be possible to infer details of the interaction of IL-4 with its cognate receptor on the basis of the structural alignment of IL-4 and HGH presented above (Fig. 10).

By analogy with the HGH–receptor complex, we therefore propose that there are two distinct sites of interaction on IL-4. The interaction site for the first receptor molecule would involve the surface formed mainly by helix α_D, strand β_A, and the loop connecting strand β_A to helix α_B (lower left-hand side of Figs. 6A and 6B and bottom of Fig. 6C), while the interaction site for the second receptor molecule would involve the surface formed by helices α_A and α_C (lower right-hand side of Figs. 6A and 6B and top right of Fig. 6C). The structure-based sequence alignment in Fig. 11, which is restricted principally to the helical regions, then permits one to infer potential residues of IL-4 involved in contacting the two receptor molecules by direct analogy with the HGH system. Residues comprising the first site in HGH are His-18 in helix α_A and Arg-167, Lys-168, Asp-171, Thr-175, and Arg-178 in helix α_D, which correspond to Asn-19, Glu-114, Asn-115, Glu-

118, Thr-122, and Arg-125, respectively, in IL-4. In addition to these residues, we would predict the potential involvement in IL-4 of Lys-121, Glu-126, and Tyr-128. Residues constituting the second site in HGH are Asn-12, Leu-15, Arg-16, and Arg-19 in helix α_A and Asp-116 and Glu-119 in helix α_C, which correspond to Glu-13, Lys-16, Thr-17, Ser-20, Arg-89, and Arg-92, respectively, in IL-4. Other likely residues at this site that could potentially make contact with the IL-4 receptor are Thr-10 in helix α_A and Asn-93 in helix α_C.

Three mutational studies are of interest in light of the above prediction. First, analyses of a series of human-mouse GM-CSF chimera have indicated that residues 21–31 and 78–94, which correspond to the second interaction site described above, are important for recognition (48). Second, site-specific mutagenesis data on GM-CSF have indicated a critical role for Glu-21 (equivalent to Glu-13 in IL-4; cf. Fig. 11) in high-affinity binding to the β-receptor chain (49). Third, a mutation in the first interaction site of Tyr-128 to Asp in IL-4 results in the generation of a competitive IL-4 antagonist which still binds to the receptor with high affinity (~60% of wild-type) but no longer possesses any proliferative activity for T cells (50).

It could be argued that the effect of the Tyr-128 → Asp mutation in IL-4 arises from the removal of an important hydrophobic interaction with the receptor molecule. This is unlikely since the aromatic ring of Tyr-128 has only limited surface accessibility (~50 Å²) and only the hydroxyl group is directly solvent exposed (Fig. 7C). If the interaction of the hydroxyl group with the receptor molecule would be crucial for IL-4 activity, one would spec-
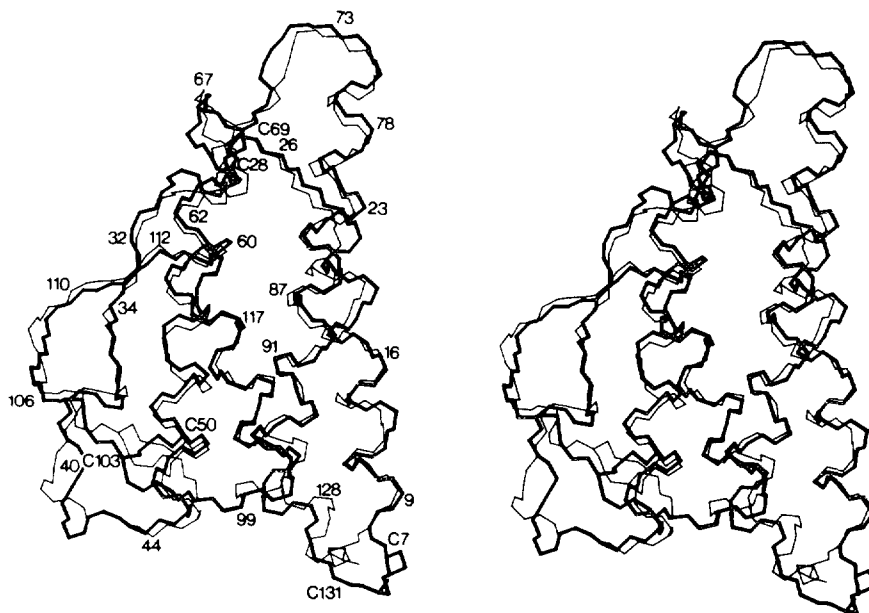

FIG. 9. Best-fit superposition of the backbone (N, C$^\alpha$, C) atoms of the restrained minimized mean NMR (thick lines) structure and the X-ray (thin lines) structure of recombinant human IL-4 for residues 7–131. The NMR and X-ray structures are from Refs. 35 and 36, respectively. Note that the natural IL-4 sequence starts at residue 5. From Ref. 35.

ulate that adding the negative-charged Asp residue might actually *increase* the stability of the interaction or at the least have no effect. In fact, replacing Tyr-128 by a positively charged Lys resulted in a mutant with a higher level of activity than the Tyr-128 → Asp mutant (50). In addition, complete removal of the hydroxyl group in the Tyr-128 → Phe mutant resulted in a protein for which complete activity and binding affinity were preserved (50). This indicates that the effect of the Tyr-128 → Asp mutation is probably not the result of a direct loss of a specific

interaction with the receptor molecule, but in all likelihood arises from a local loss of structural integrity of IL-4, a very likely occurrence given the fact that the side chain at position 128 resides on the interior face of the helix.

Tyr-128 is the C-terminal residue of helix α_D which is part of the first proposed binding site. Any local unwinding or disruption of helix α_D could be severe enough to eliminate this binding site. There is a significant amount of evidence that suggests that electrostatic interactions
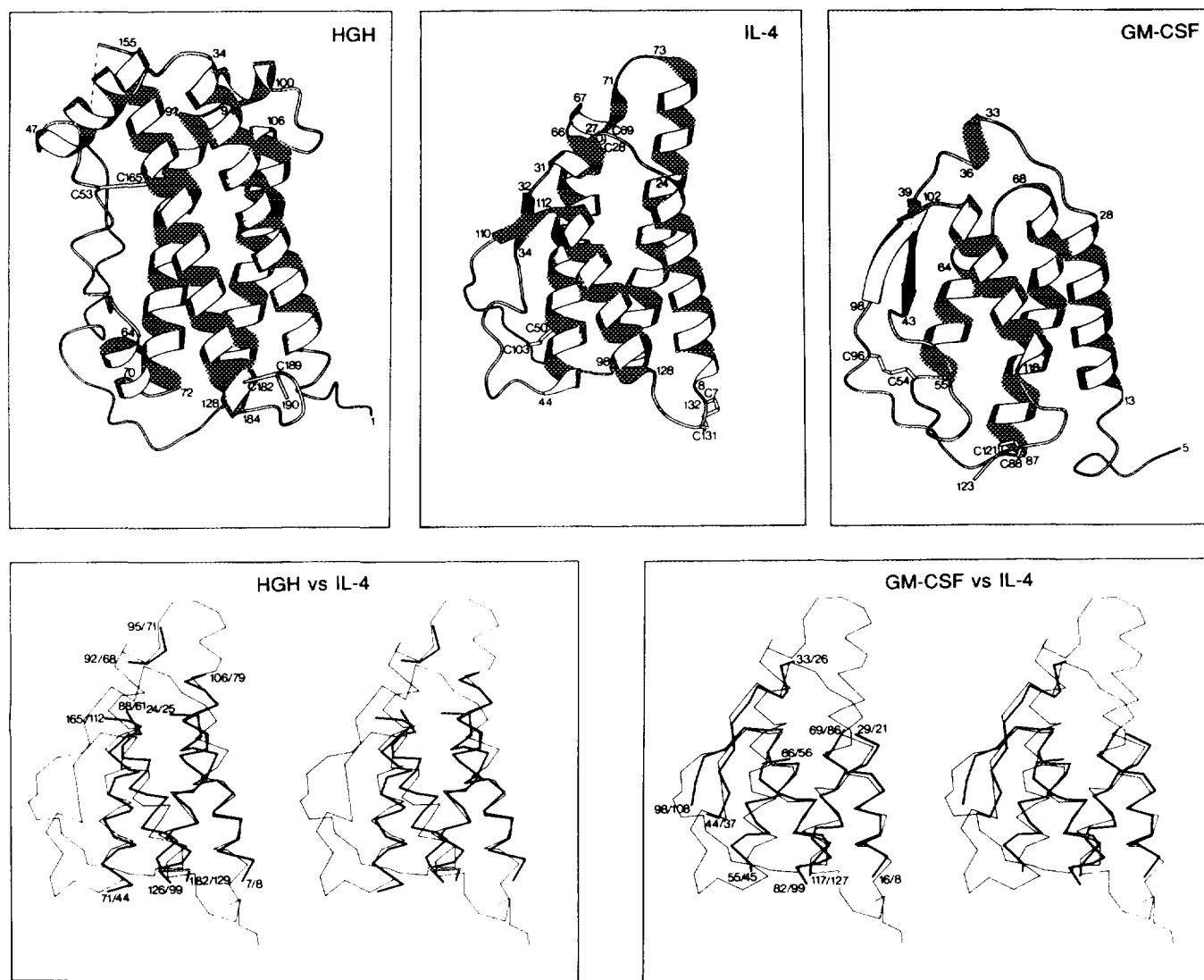

FIG. 10. Ribbon drawings of the restrained minimized mean NMR structure of recombinant human IL-4 and the X-ray structures of human growth hormone (HGH) and granulocyte–macrophage colony-stimulating factor (GM-CSF) are shown in the top three panels. Residues 7–132 are shown for IL-4, residues 1–190 for HGH, and residues 5–123 for GM-CSF. The three disulfide bridges in IL-4 and the two disulfide bridges in HGH and GM-CSF are labeled along with the beginning and end of the helical regions. In the bottom two panels, best-fit superpositions of the C^α atoms of the restrained minimized mean NMR (thin lines) structure of IL-4 with the C^α atoms of the matched residues of the X-ray structures (thick lines) of HGH (79 residues) and GM-CSF (72 residues) are shown. The residue numbers at the beginning and end of each fragment are indicated, with the first number corresponding to HGH or GM-CSF and the second to IL-4. Note that the natural IL-4 sequence starts at residue 5. The ribbon diagrams were generated with the program Molscript (69). The NMR structure of IL-4 is from Ref. 35 and the X-ray structure of HGH and GM-CSF are from Refs. 39 and 41, respectively. From Ref. 35.

are important in α-helix formation (51). These results suggest that the presence of appropriate charged groups at the N- and C-termini of a helix can interact favorably with the positive and negative poles, respectively, of the α-helix macrodipole, thereby stabilizing the helix. Therefore, by analogy, the mutation of Tyr-128 to the negatively charged Asp residue probably destabilizes helix α_D because of its unfavorable interaction with the negative pole of the α-helix macrodipole. Indeed, the probability of finding an Asp residue at the C-terminus of an α-helix in native proteins is very low (51). This also explains why the Tyr-128 → Lys mutation has a higher relative activity than the Tyr-128 → Asp mutation, since the positively charged Lys would interact favorably with the negative pole of the helix macrodipole. Even though the Tyr-128 → Lys mutation probably stabilizes the formation of helix α_D, the mutant is significantly less active than native IL-4, presumably because of a conformational effect on receptor binding due to the introduction of a positive charge at this location. The Tyr-128 → Asp mutation is obviously only severe enough to eliminate one receptor binding site, consistent with the 60% decrease in receptor binding affinity (50). (Note that the stoichiometry of receptor binding for the wild-type and mutant proteins was not established.) The other mutations at position 128 (Phe, His, Asn, Lys, Gly) all have receptor binding affinity similar to that of wild-type IL-4, but exhibit varying degrees of reduced biological efficacy. This suggests that the effects of these various Tyr-128 mutations result in only local structural perturbations affecting a single receptor binding site. Hence, the observation that the Tyr-128 → Asp mutation eliminates IL-4 efficacy and acts as an antagonist is consistent with the view that signal transduction in the IL-4 system involves multiple binding sites on IL-4, possibly causing receptor dimerization. Thus, the antagonist properties of the Tyr-128 → Asp mutant appear to arise from the loss of one binding site and the concomitant prevention of receptor dimerization.

INTERLEUKIN-8

Interleukin-8 (IL-8), also variously known as neutrophil activation factor or protein (NAP-1), monocyte-derived neutrophil chemotactic factor, mitogen-stimulated human leukocyte protein, and T-cell chemotactic factor, is a dimeric protein (52, 53) composed of two identical subunits, each of 8 kDa, and is released from several cell types, including monocytes, fibroblasts, endothelial cells, and keratinocytes, in response to an inflammatory stimulus (54). IL-8 production via an increase in IL-8 mRNA synthesis is stimulated by both interleukin-1 and tumor necrosis factor, as well as exogenous factors such as lipopolysaccharide and the nonspecific mitogen phytohemagglutinin. A range of in vitro and in vivo studies have shown that IL-8 displays two major biological activities. The first is the selective capacity to attract neutrophils, basophils, and T cells, but not monocytes. The second involves neutrophil activation via the elevation of cytosolic calcium, the stimulation of the respiratory burst response, superoxide generation, and the release of lysosomal enzymes. IL-8 also causes rapid induction of Mac-1 expression on neutrophils, which probably contributes to increased adhesion of neutrophils to vascular endothelial cells, and recently it has been shown that IL-8 stimulates the release of histamine from basophils.

Sequence comparisons have revealed that IL-8 belongs to a protein superfamily whose members are involved in cell-specific chemotaxis, mediation of cell growth, and the inflammatory response (54, 55). All members of this superfamily are composed of polypeptide chains of approximately 8–10 kDa and contain four cysteine residues at
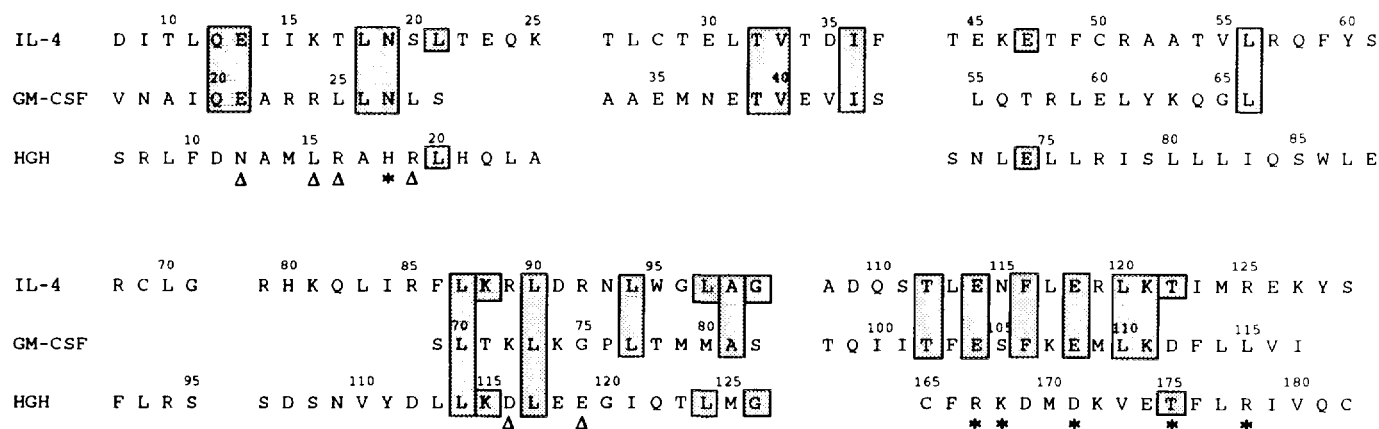

FIG. 11. Sequence alignment of IL-4, HGH, and GM-CSF based on the structural superposition shown in Fig. 10. The asterisks and triangles indicate the residues of HGH that interact with the first and second receptor molecules, respectively, in the X-ray structure of the HGH–receptor complex. Sequence identities are indicated by shaded boxes. Note that the natural human IL-4 sequence starts at residue 5. From Ref. 35.

near identical positions. This superfamily of proteins has been further subdivided into two distinct subfamilies. The first is the β-thromboglobulin (β-TG) subfamily which comprises, among others, platelet factor 4 (PF4), interferon-γ-induced protein (γIP-10), growth-related gene product/melanoma growth-stimulating activity (GRO/MGSA), macrophage inflammatory protein 2 (MIP-2), and IL-8. In this subfamily the first two cysteine residues are separated by a single residue in a Cys–X–Cys pattern, while in the second subfamily they are adjacent to each other (i.e., Cys–Cys). Members of the second subfamily include monocyte chemoattractant protein 1, which is the product of the human JE gene (MCP-1/JE), also known as monocyte chemotactic and activating factor (MCAF); macrophage inflammatory protein-1 (MIP-1); RANTES; and the product of an immune activation gene (Act-2). Members within each subfamily exhibit 25–55% sequence identity, and the amino identity between members of the two subfamilies ranges from 21 to 31%, clearly indicating an evolutionary and functional relationship between all proteins belonging to both subfamilies.

The high-resolution structure of IL-8 has been determined in solution on the basis of 1880 experimental NMR restraints (56). The X-ray structure at 2 Å resolution was subsequently solved *by necessity* using the NMR structure as a starting model for molecular replacement, as other methods proved unsuccessful (57). In particular, no suitable heavy-atom derivatives for isomorphous replacement could be obtained despite several years of effort, and molecular replacement using the crystal structure of the homologous protein bovine PF4 (58) failed.

The Solution Structure of IL-8

Two views of the polypeptide fold of the IL-8 structure in solution are shown in Fig. 12. The approximate overall dimensions of the IL-8 dimer are 30 × 26 × 18 Å. The structure essentially consists of two antiparallel α-helices lying on top of a six-stranded antiparallel β-sheet. The surface under the β-sheet is concave and, except for Ile-28 and Ile-40, is composed entirely of hydrophilic and charged residues. The two symmetry-related helices are ~24 Å long and are separated by a center-to-center distance of 14.8 Å. The view of IL-8 shown in Fig. 12A and 12B is one looking down the C_2 symmetry axis, which is located in the center of the β-sheet halfway between the C^α atom positions of Arg-26 of the two subunits. The orientation depicted in Fig. 12C demonstrates most strikingly the exposed position of the two α-helices on top of the molecule.

The topology and hydrogen-bonding pattern of IL-8 are depicted schematically in Fig. 13. Within each subunit, the main secondary structure elements comprise a long C-terminal helix extending from residues 56 to 72 and a triple-stranded antiparallel β-sheet arranged in a Greek key, in which strand 1 (residues 23–30) is hydrogen bonded to strand 2 (residues 36–43), which in turn is hydrogen

bonded to strand 3 (residues 48–51). The disulfide bridge between Cys-7 and Cys-34 is right-handed, while that between Cys-9 and Cys-50 is left-handed. At the N-terminus a series of nonclassical turns at residues Gln-8/Cys-9, Ile-10, Lys-11, and Ser-14 make up a long loop extending from Gln-8 to His-18. This is followed by a single 3–10 helical turn formed by residues 19–22 which leads into strand 1. Strands 1 and 2 are connected by a rather unusual turn or loop with a kink at Ser-30 and Ala-35 and two hydrogen bonds between the backbone amides of Gly-31 and Cys-34 and the carbonyl atoms of Cys-34 and Gly-31, respectively. The glycine at position 31 is either conserved or substituted conservatively in all members of the IL-8 superfamily. Similarly, the conformation of the turn (residues 43–47) connecting strands 2 and 3 is rather unusual and falls into the classification of a 3:5 type I turn with a G1 β-bulge. The residue at position 4 of the turn is a glycine (Gly-46) which is conserved in PF4, β-TG, GRO/MGSA, and γIP-10 and substituted conservatively by either an Asp or a Ser in other members of the protein superfamily. Strand 3 leads into the helix via a type I turn from residues 52–55 which is stabilized by two hydrogen bonds: a backbone NH(Glu-55)–CO(Asp-52) hydrogen bond and a hydrogen bond between the backbone amide of Lys-54 and the carboxylate side-chain group of Asp-52.

The orientation of the helix relative to the triple-stranded β-sheet within each monomer is stabilized by a number of hydrophobic interactions (Fig. 14). In particular, the six-member ring of Trp-57 is perfectly packed on top of the ring of Pro-16 (Fig. 14A) and is also in close contact with Tyr-13, Phe-17, and Leu-51. Additionally, Phe-65 is in van der Waals contact with Pro-19, Ile-22, and Leu-25, Val-58 with Ile-39 and Leu-51, Val-61 with Pro-19, and Val-62 with Ile-22.

The dimer interface is stabilized principally by an antiparallel β-sheet with six hydrogen bonds between strand 1 of one subunit and strand 1' of the second (Fig. 13). In addition to these backbone hydrogen bond interactions, there are a number of other stabilizing forces involving side chains (Fig. 14B). In particular, there are hydrophobic contacts between Phe-65 of the C-terminal helix of one subunit and the methyl groups of Val-27 and Thr-37 of the second. There is also an electrostatic interaction between the two helices involving Gln-59 of one subunit and Glu-70 of the other. These interactions further serve to maintain the orientation of the C-terminal helices, with respect both to each other and to the β-sheet below. The upper face of the β-sheet, which is in contact with one face of the α-helices, is entirely hydrophobic, and there are hydrophobic interactions between residues of strand 1 from the two subunits, in particular between Leu-25 of one subunit and Val-27 of the other. Finally, there is an electrostatic interaction on the bottom of the β-sheet between Glu-24 of one subunit and Arg-26 of the other.

Comparison of IL-8 in the Solution and Crystal States

The overall molecular architecture and backbone hydrogen bonding of the NMR and X-ray structures are essentially identical (Fig. 15). The backbone atomic rms difference between the monomer units of the NMR and X-ray structures is 1.1 Å for residues 7–72 (59) and there is good correspondence in the conformations of the internal side chains.

The backbone atomic rms difference between the two structures for the dimer, however, is significantly larger (~2 Å) and is due to a difference in the relative orientation of the two subunits (59). This is discussed in detail below.
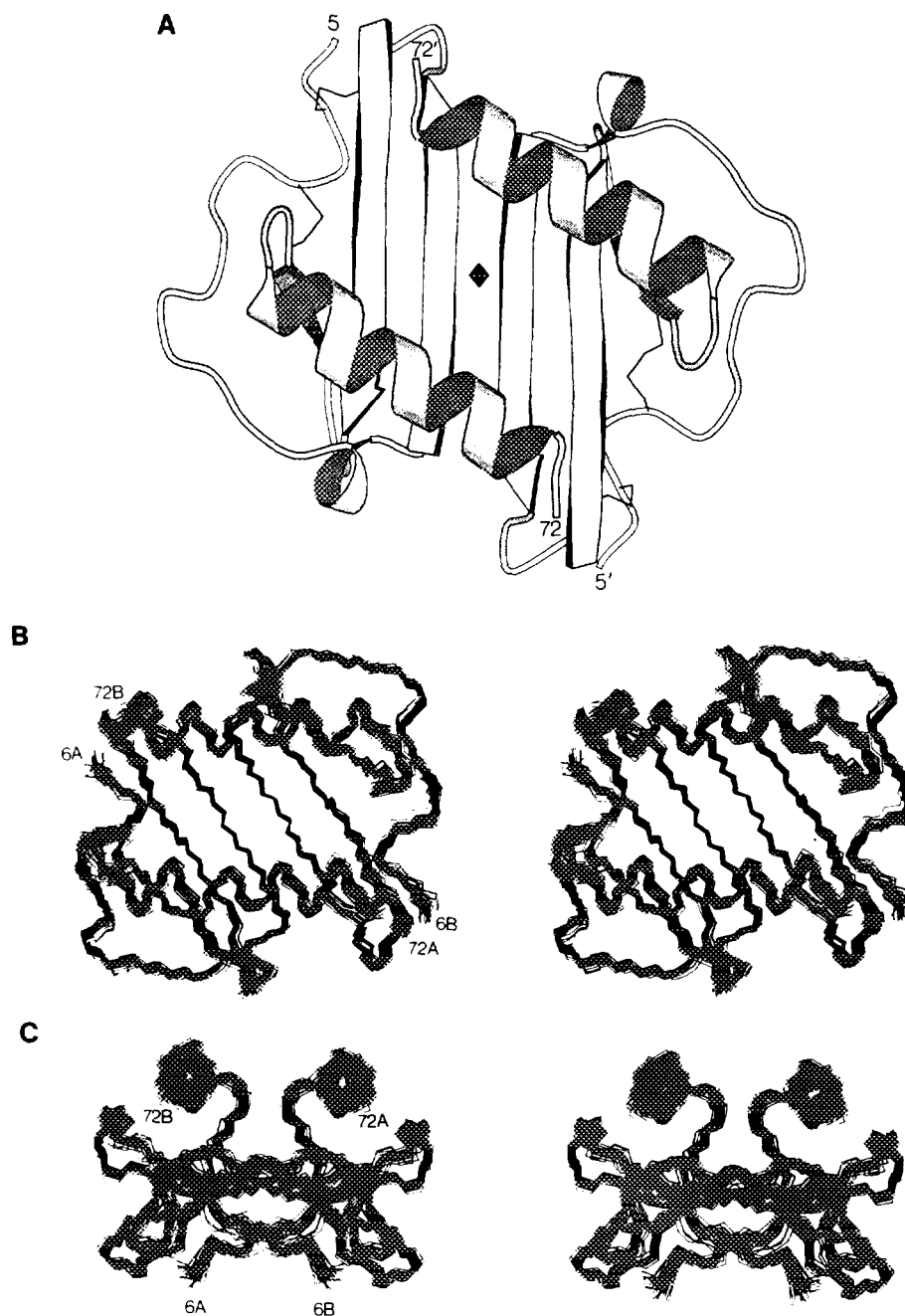
FIG. 12. (A) Schematic ribbon drawing of the solution structure of IL-8. The diamond indicates the location of the C_2 axis. (B, C) Two stereoviews showing superpositions of the backbone (N, C^α, C) atoms of the 30 calculated NMR structures. The average atomic rms distribution of the 30 structures about their mean coordinate positions for residues 6–72 is 0.41 ± 0.08 Å for the backbone atoms, 0.90 ± 0.08 Å for all atoms, and 0.50 ± 0.08 Å for all atoms of internal side chains (surface accessibility ≤100 Å^2). The N-terminus (residues 1–5) is disordered in solution. The ribbon drawing in (A) was generated using the program Molscript (69). Adapted from Ref. 56.

At the monomer level, there are two regions where the structure of IL-8 differs significantly in the solution and crystal states, namely, at the N-terminus and in the loop connecting strands 1 and 2 (Figs. 15 and 16) (59). At the N-terminus residues 4–6 are ill-defined in the NMR structure but well defined in the X-ray structure, and the X-ray structure predicts a number of short interproton distance contacts <3.5 Å between Glu-4 and His-33, between Leu-5 and Gln-8, and between Leu-5 and His-33, which are not observed in solution. Also present in the X-ray structure is a salt bridge between the carboxylate of Glu-4 of one subunit and the $N^\zeta H_3^+$ group of Lys-23 of the other subunit (Fig. 15B). This electrostatic interaction

fixes the conformation of the N-terminal residues in the X-ray structure. In the NMR structure, on the other hand, residues 4–6 are not well ordered, although it is apparent from Figs. 15 and 16A that the polypeptide chain at the N-terminus runs in different directions in the two structures, and the electrostatic interaction observed in the crystal structure is completely absent in solution and replaced by an electrostatic interaction between the carboxylate of Glu-29 of one subunit and the $N^\zeta H_3^+$ group of Lys-23' of the other subunit.

The second region of substantial difference between the two structures within the monomer unit relates to the location of the loop formed by residues 31–36 (Fig. 16).
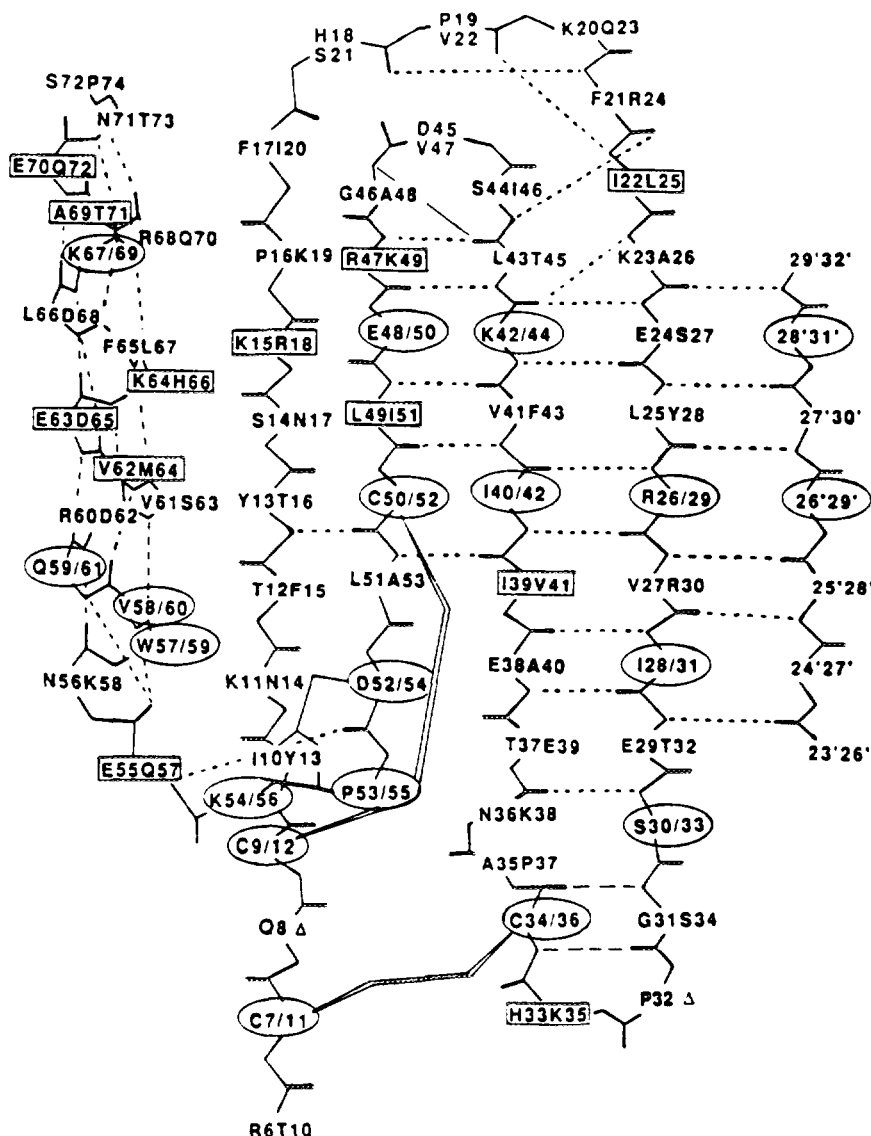

FIG. 13. Schematic illustration of the secondary structure and topology of IL-8 together with the aligned sequence of MCAF/MCP-1. The residue of IL-8 is listed first and the corresponding one of MCAF/MCP-1 second. The conserved backbone hydrogen bonds between the IL-8 structure and the MCAF/MCP-1 model based upon it are indicated by dotted lines, and those present only in IL-8 are indicated by thinner lines. From Ref. 53.

In both structures this loop is covalently attached to the N-terminal strand through the disulfide bridge between Cys-7 and Cys-34, and the difference between the two structures has its most pronounced manifestation in the presence of different interactions involving the imidazole ring of His-33 (Fig. 17). In solution, His-33 *accepts* a hydrogen bond from the backbone NH of Gln-8 (Fig. 17A), accounting for both the observed low pK_a of 4.9 for His-33 and the extreme downfield chemical shift of the NH of Gln-8 that resonates at ~12 ppm. In contrast, in the crystal structure the $N^{\epsilon 2}H$ atom of His-33 *donates* a hydrogen bond to the backbone carbonyl group of Glu-29 (Fig. 17B). This, together with the absence of any neighboring positive charge, would predict a $pK_a > 6.5$ for His-33.

In light of the different interactions involving His-33 in the NMR and X-ray structures, it is interesting to note that the second histidine in IL-8 at position 18 also has an extremely low pK_a of 3.7, and in both structures the imidazole $N^{\delta 1}$ atom *accepts* a hydrogen bond from the backbone NH of Lys-20. Like Gln-8, the NH of Lys-20 also exhibits an extreme downfield shift.

The origin of the different conformations of the 31–36 loop in the two structures may be attributed to two factors. First, in the crystal structure Pro-32 is tightly packed in a hydrophobic pocket formed by Tyr-13, Phe-17, Phe-21, and Leu-43 of an adjacent molecule in the crystal lattice, and the position of the carbonyl of Pro-32 is further fixed by an electrostatic interaction with the side chain of Arg-47 of a neighboring molecule. Second, the salt bridge between Glu-4 of one subunit and Lys-23' of the other in the crystal structure prevents the loop, and in particular His-33, from coming into hydrogen-bonding range of the NH of Gln-8.

At the quaternary level there is a significant difference in the relative orientation of the two subunits in the solution and crystal states (Fig. 18). Thus, when subunit A of both structures is superimposed, the backbone atomic rms shift between subunit B of the two structures is ~4.4
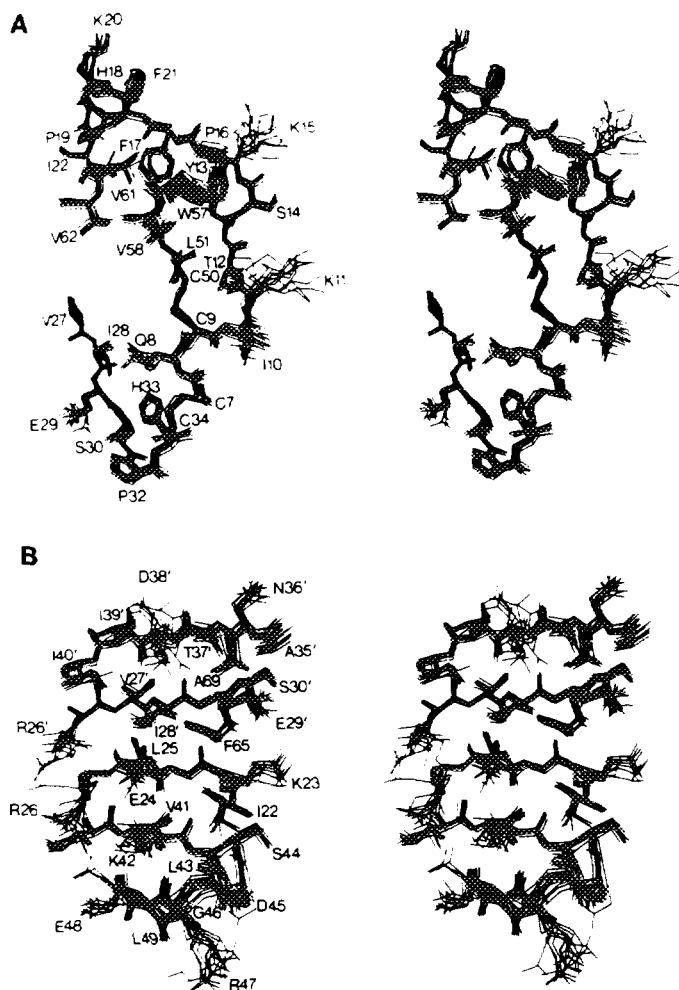

FIG. 14. Stereoviews showing best-fit superpositions of all atoms (excluding protons) of 15 calculated NMR structures of IL-8 for two selected segments of the protein. From Ref. 56.
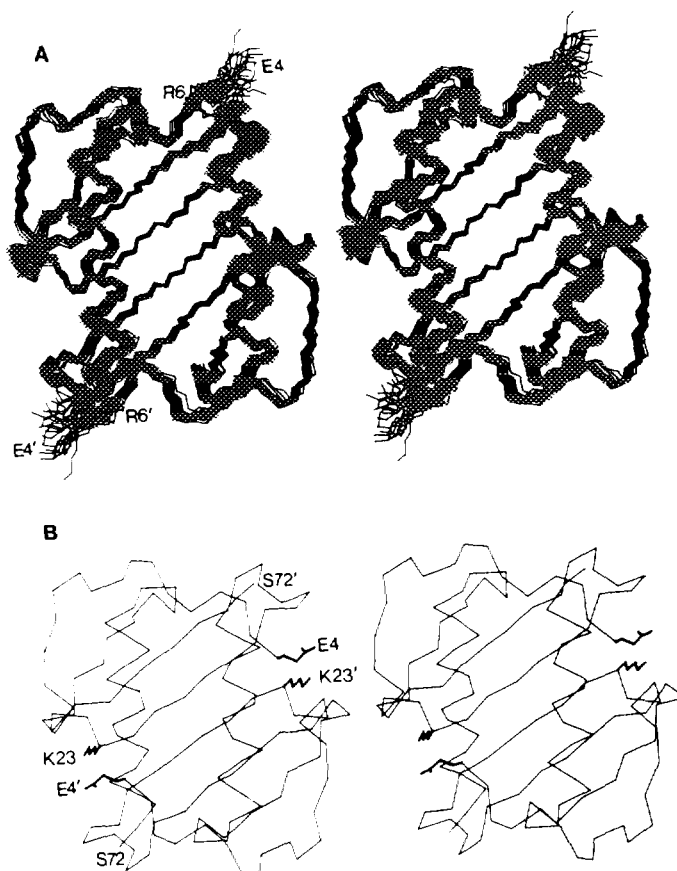

FIG. 15. (A) Stereoview of the backbone atoms of the 30 calculated NMR solution structures of IL-8 and (B) stereoview of the C^α atoms of the X-ray structure of IL-8 together with the side chains of Glu-4 and Lys-23. From Ref. 59.

Å. Differences of similar magnitude in the orientation of one subunit or domain relative to another have been observed in crystal structures of the Bence–Jones protein Loc (60), in the catabolite activator (or cyclic AMP receptor) protein (61), in a mutant of T4 lysozyme (62), and in cro free and complexed with DNA (63).

The main result of the difference in quaternary structure is that the separation and angle between the long axes of the two helices are 14.8 Å and 172° in the solution structure versus 11.1 Å and 164° in the crystal structure. In this regard it must be emphasized that the relative orientation of the two subunits in the solution structure is determined only by the experimental NMR restraints, as the nonbonded term of the target function minimized by simulated annealing is represented *solely* by a quartic van der Waals repulsion term, and *no* Lennard–Jones, electrostatic, or hydrogen-bonding terms are used in the NMR structure calculations (56, 59). The X-ray structure also predicts another 30 short interproton distance contacts less than 4 Å between the two subunits which are not observed experimentally in solution. Thus, when the crystal structure is subjected to simulated annealing against a target function comprising the experimental NMR restraints, it is converted back into a structure that falls well within the envelope of the individual simulated annealing NMR structures. The origin for this difference is seen in Fig. 18 and arises from the different angle between the long axes of the two central strands of the β-sheet at the dimer interface formed by residues 23–29 of the two subunits. Whereas in the solution structure of

IL-8, these two strands are at an angle of ~168°, commonly found in regular β-sheets, in the IL-8 crystal structure the central sheet is virtually flat with an angle of ~179°. In contrast, the angles between strands 1 and 2 and between strands 2 and 3 are essentially the same in the solution and crystal structures, with values typical of a classical β-sheet. Because the direction of the helices is almost orthogonal to that of the strands, the actual angle being around 60°, a reduction in the angle between the axes of the central strands brings the helices closer together and decreases the angle between their long axes. Thus, the difference in quaternary structure can be attributed to a rigid body rotation of the two subunits about the C_2 axis of symmetry. Inspection of the two structures suggests that the difference in the twist of the central β-strands is related to the two differences at the monomer level, which were described above, acting in synergy. Thus, the relative orientation of the two strands is affected by interactions at both the N- and C-terminal ends of the strands, in particular the electrostatic interaction between Lys-23' of one subunit and the carboxylate group of either Glu-29 (NMR) or Glu-4 (X-ray) of the other, and the hydrogen-bonding interaction of His-33 with either the backbone amide of Gln-8 (NMR) or the backbone carbonyl of Glu-29 (X-ray).

Modeling of MCAF/MCP-1 based on the 3D NMR Structure of IL-8

Also shown in the schematic structural representation in Fig. 13 is the sequence alignment with a member of
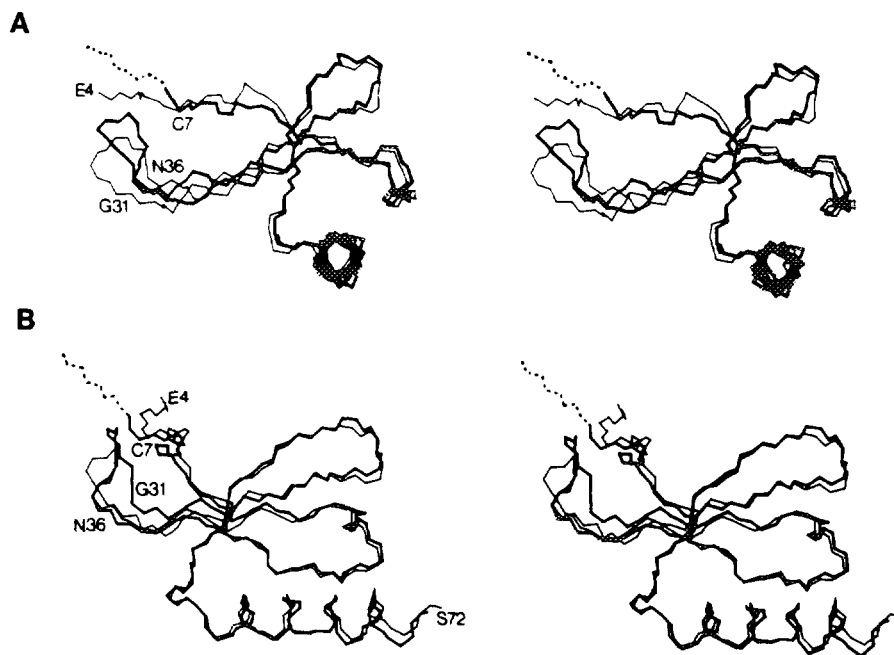

FIG. 16.   Two stereoviews showing superpositions of the backbone (N, C^α, C) atoms of the monomer unit of the restrained minimized mean NMR (thick lines) and X-ray (thin lines) structures of IL-8. From Ref. 59.

the second subfamily, MCAF/MCP-1, based on considerations of the secondary and tertiary structure of IL-8 (64). The MCAF/MCP-1 sequence (76 residues) is readily aligned starting at residue 5 with that of IL-8 (72 residues) incorporating two single amino acid deletions corresponding to positions 8 and 32 in the IL-8 sequence, resulting in sequence identity for 17 of the 72 residues (i.e., 24% sequence identity) and conservative changes for an additional 12 residues. The latter only include those pairs that belong to groups exhibiting the same charge and hydrophobic properties, as well as similar size. If a somewhat more generous interpretation of conservative changes is taken into account, including, for example, Glu/Ala, Glu/Thr, Glu/Ser, Leu/Phe, Ile/Phe, and Val/Phe pairs, then the entire triple-stranded β-sheet would contain only conserved residues. It is also interesting to note that the amino acid substitution Glu-29 → Thr-32 is accompanied by the reverse substitution Thr-37 → Glu-39 and that these two amino acids are located opposite each other on two antiparallel β-strands, pointing upward from the sheet in the direction of the helices (Fig. 19). Thus, the space occupied by these amino acid side chains is identical in both proteins. Homology modeling followed by energy minimization indicates that it is easily possible to accommodate all the interior side chains in MCAF/MCP-1 with minimal disturbance of the general IL-8 polypeptide fold. Thus, the atomic rms difference for the backbone atoms between the IL-8 NMR structure and the modeled MCAF/MCP-1 structure is only 0.9 Å, and there are no significant differences in either the values of the non-

bonding energies or in the deviations from idealized geometry between the two structures. Remaining bad steric clashes would almost certainly be reflected by a higher van der Waals energy, and the fact that the energetics of the modeled structure are very similar to those of the IL-8 NMR structure can be taken as an indication that good packing within the protein interior has been achieved.

In the final modeled structure of MCAF/MCP-1 most backbone hydrogen bonds in the regular secondary structure elements that are present in IL-8 are retained. The hydrogen bonds within the two turn regions connecting strands 1 and 2 and strands 2 and 3 (residues 31–34 and 43–47, respectively, in IL-8) are no longer present in the MCAF/MCP-1 structure. The loop around Cys-34/-36 quite clearly must have a somewhat different conformation given that the proline at position 32 in IL-8 is deleted in MCAF/MCP-1 and a sequence change Ala-35/Pro-37 occurs as well. The 3:5 β hairpin loop connecting strands 2 and 3 in IL-8 is retained in the modeled structure, although typical turn residues Asn and Gly are replaced by Val and Ala.

The disulfide bridge between Cys-9/12 and Cys-50/52 can be directly superimposed in the two structures and is a classical left-handed spiral conformation. The second disulfide bridge between Cys-7 and Cys-34 is a right-handed hook in the IL-8 structure. In MCAF/MCP-1 the corresponding disulfide bridge between Cys-11 and Cys-36 can readily be modeled in a classical left-handed conformation.
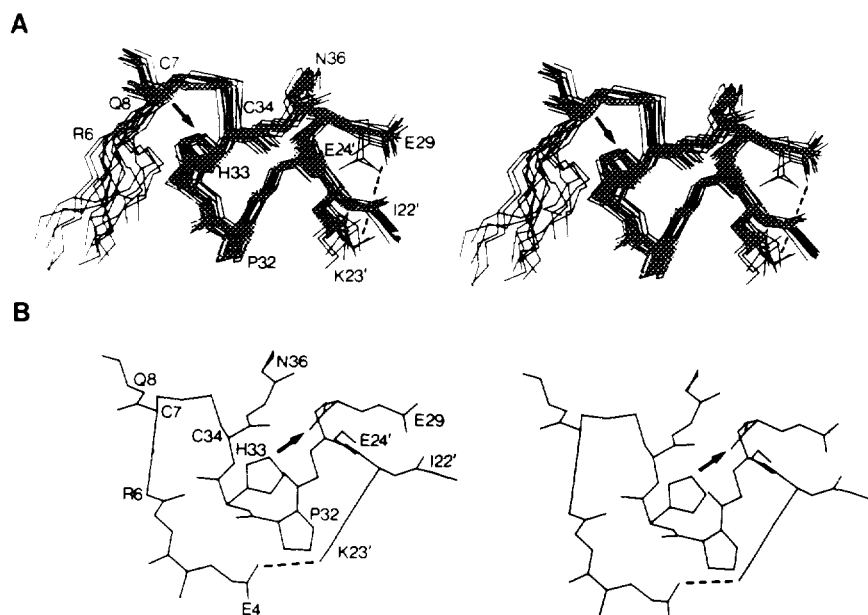

FIG. 17. Comparison of the 31–36 loop and its associated interactions in the NMR and X-ray structures of IL-8. (A) Superposition of 15 calculated NMR structures; (B) view of the X-ray structure in the same orientation. The arrows indicate hydrogen bonds involving the imidazole ring of His-33 and the dashed lines indicate electrostatic interactions. From Ref. 59.

The helical turn between residues 18 and 22 in IL-8, which is stabilized in part by the hydrogen bond between the $N^{\delta 1}$ imidazole atom of His-18 and the backbone amide of Lys-20, is preserved in MCAF/MCP-1 by an equivalent interaction between the $O^{\gamma 1}$ atom of Ser-21 (replacing the $N^{\delta 1}$ imidazole atom of the histidine) and the backbone amide of Gln-23.

As discussed above, the positioning of the long α-helix on top of the β-sheet in IL-8 is achieved by a specific set of hydrophobic interactions. This kind of van der Waals interaction is also maintained in the modeled structure of MCAF/MCP-1 and simply involves a different set of hydrophobic side chains. Thus, Trp-59 in MCAF/MCP-1 (which is equivalent to Trp-57 in IL-8) is surrounded by Phe-15, Ile-20, and Ala-51. Likewise, Leu-67 in MCAF/MCP-1 (equivalent to Phe-65 in IL-8) interacts with Leu-25 and Tyr-28. These two sets of hydrophobic clusters can be retained throughout the entire superfamily since each protein sequence contains conserved hydrophobic residues at these positions.

Relationship of Structure to Function

The general architecture of the IL-8 dimer consists of a six-stranded antiparallel β-sheet spanned by two long symmetry-related α-helices at the C-terminus of the two subunits. These helices are positioned at an angle of approximately $+60°$ with respect to the orientation of the β-strands in the sheet and are separated by either 14.8 Å

in the solution structure or 11.1 Å in the crystal structure. This architecture is remarkably similar to the fold of the $\alpha 1/\alpha 2$ domains of the Class I major histocompatibility (MHC) antigen HLA-A2 determined by X-ray crystallography (65), where the sheet is formed by eight β-strands, four from each domain, with two antiparallel helices separated by ~ 18 Å running across them at an angle of $\sim -45°$. Thus, the same kind of architecture is achieved with two different kinds of β-pleated sheets in which the strands run almost orthogonal to each other. In the case of HLA-A2, the β-sheet is formed by strands arising from two domains of a single subunit (i.e., a pseudo-dimer), while in the case of IL-8 it is formed by strands originating from two separate subunits (i.e., an intermolecular dimer).

The views of IL-8 shown in Fig. 12 clearly demonstrate the prominent positioning of the two α-helices, which basically sit on top of the rather flat β-sheet domain, with hydrophobic amino acid side chains forming the central features at the α/β interface. In fact, the α-helix represents an almost idealized amphiphilic helix, with hydrophobic residues on the interior face and hydrophilic residues on the solvent-exposed face. The hydrophobic residues oriented toward the β-sheet are Val-58, Val-61, Val-62, and Phe-65, with the latter forming the central anchor of the helix. Leu-66 is located between the two helices, while Trp-57 is involved in a stabilizing interaction between the loop around Pro-16 and the other side of the helix.
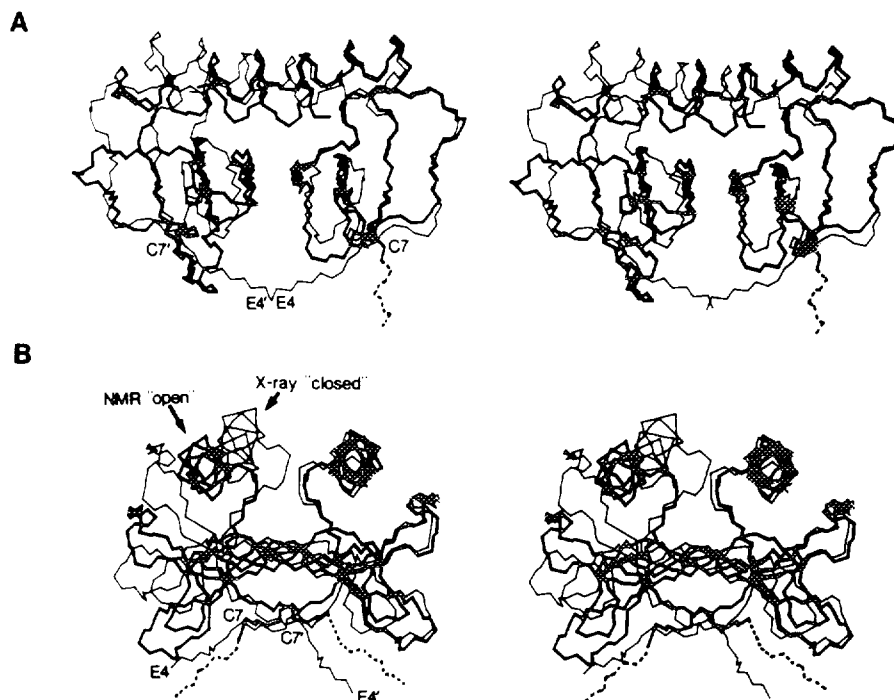

FIG. 18. Two stereoviews of best-fit superpositions (to one monomer) of the backbone (N, C$^\alpha$, C) atoms of the restrained minimized mean NMR (thick lines) and X-ray (thin lines) structures of IL-8. From Ref. 59.

The charged or polar amino acids that are solvent exposed are Asn-66, Gln-59, Arg-60, Glu-63, Lys-64, Lys-67, Glu-70, and Asn-71. Alignment of the IL-8 sequence with the sequences of the other proteins in the superfamily, based on the assumption that the structure following Cys-50, as well as the phase of the helix, is similar in all the proteins, shows that the sequences exhibit amphiphilic properties of a potential α-helix with strong conservation of hydrophobic residues for those positions that are found at the α/β interface in IL-8 and PF4.

In light of the striking structural similarities between the α1/α2 domains of HLA-A2 and IL-8, it is tempting to speculate on the functional role of the two antiparallel helices in IL-8 and the cleft between them. In HLA-A2 the antigen recognition site and T-cell receptor interaction reside in the region between and comprising the two approximately antiparallel α-helices (65, 66). While the α1 and α2 domains of HLA-A2 are not identical, they are similar, and the two α-helices are related by a pseudo-dyad. In the case of IL-8, the two subunits are identical and the two α-helices are located symmetrically about the dyad axis. It therefore may well be that the two long α-helices in IL-8 and the other members of the superfamily serve as a major interaction site with their respective receptor. Specific recognition would then be achieved in part through different combinations of polar and charged residues on the outside of the helix which would have their counterparts on the surface of the cellular receptor. The residues that are likely to be important here are located at positions 59, 60, 63, 64, and 67. In this regard it is interesting to note that IL-8 and GRO/MGSA display the same biological activities and the only changes in any

of these residues are conservative (Arg-60 → Lys and Glu-63 → Gln), preserve functional groups, and do not cause charge reversal. In contrast, PF4 does not bind to the IL-8 receptor, which may possibly be accounted for in part by an alteration in charge at positions 63 (Glu → Lys) and 67 (Lys → Asp).

The other residues that are clearly going to be important in receptor binding are those located in the cleft between the two helices, namely, those at positions 25, 27, and 66. In the IL-8 subfamily the residues at positions 25 and 27 are always hydrophobic (Leu or Val), whereas in the MCAF/MCP-1 subfamily they are hydrophilic (Tyr) and polar (Arg, Glu, Lys), respectively. The residue at position 66 is usually hydrophobic in the IL-8 subfamily (Leu, Met), but invariably hydrophilic and usually charged in the MCAF/MCP-1 subfamily (Asp, Glu). These differences within the cleft, as well as the single charge inversion at position 60 (Arg → Asp), coupled with the replacement of the $N^\zeta H_3^+$ functional group of Lys-64 by the imidazole ring of a histidine may account for the differential chemotactic activity of MCAF/MCP-1 and IL-8, the former for monocytes and the latter for neutrophils, basophils, and T cells. This has recently been confirmed by a mutagenesis study in which it was shown that the double Tyr-28 → Leu and Arg-30 → Val (equivalent to positions 25 and 27 of IL-8) mutant of MCAF displays a drastic decrease in chemotactic activity toward monocytes and the appearance of IL-8-like neutrophil chemotactic activity (67).

Although the difference in quaternary structure between the solution and crystal states of IL-8, "open" with a large interhelical cleft versus "closed" with a small in-
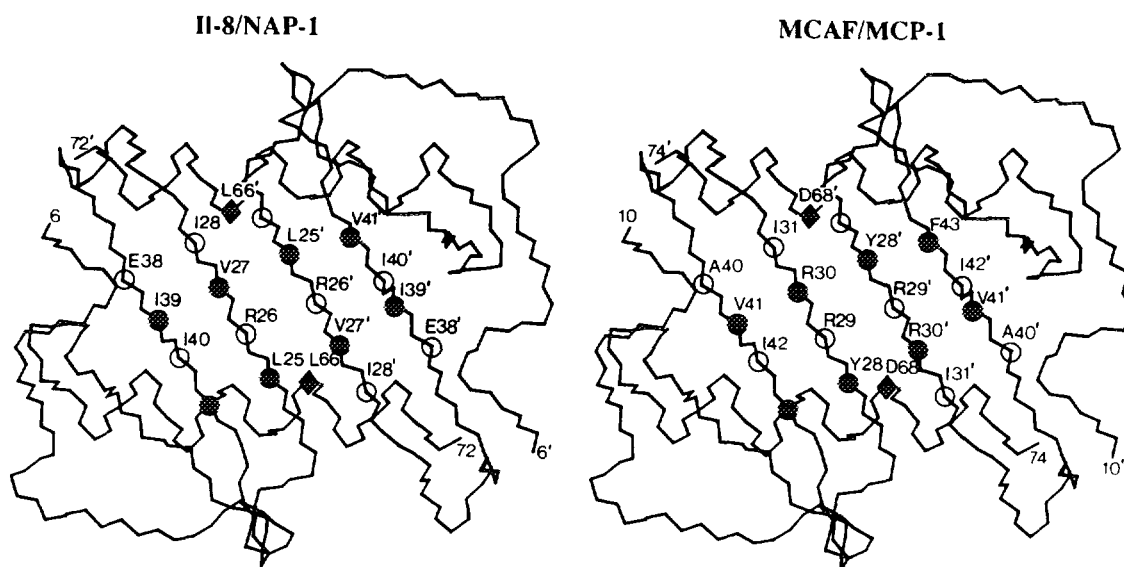
IL-8/NAP-1   MCAF/MCP-1

FIG. 19. Schematic illustration of the distribution of amino acids in the floor of the cleft between the two long α-helices for IL-8 and MCAF/MCP-1. Open circles represent residues pointing down from the β-sheet; filled-in circles, residues pointing upward from the β-sheet into the cleft; and filled-in diamonds, residues pointing into the cleft. From Ref. 64.

terhelical cleft, respectively, may arise purely from crystal lattice forces favoring one conformation over another, the observation of these different states indicates that IL-8 has the potential to undergo conformational transitions. On the basis of the arguments put forward above, we propose that these differences may be of functional significance. This hypothesis suggests a possible avenue for the rational design of IL-8 inhibitors because it predicts that any molecule that would inhibit the quaternary conformational changes from taking place would also inhibit IL-8 from eliciting its usual biological response. Such an inhibitor need be directed to bind not only to the helices and the cleft between them, but also to parts of the N-terminus (Glu-4 to Cys-9) and the 31-36 loop, both of which form a single contiguous surface projecting from the edge of the β-sheet into solution and are structurally related to the differences in quaternary conformation as discussed above. The possible relevance of these residues with regard to the mechanism of action of IL-8 is suggested by sequence comparisons of IL-8, GRO/MGSA, and murine MIP-2, all of which bind to the same receptor on neutrophils and elicit an identical response. In particular, the two stretches of residues from Glu-4 to Cys-9 and from Gly-31 to Cys-34 are conserved in all three proteins (Fig. 1), and the residue at position 23, either a Lys (IL-8) or a Gln (GRO/MGSA and MIP-2), can potentially take part in an electrostatic interaction with Glu-4 of the other subunit. PF4 from various sources, on the other hand, displays only weak neutrophil chemotaxis activity (68). Apart from the effect of a number of substitutions at the surface of the two helices that result in two charge alterations (see above), it may well be the case that PF4 cannot undergo the conformational transition between the open and closed states as Glu-4 is substituted by an Asp and Lys-23 by a Ser or Thr. Both of these side chains are too short to permit any significant electrostatic interaction between them. Hence, the quaternary structure of PF4 remains similar to that of the open form of IL-8 represented by the solution NMR structure. This interpretation is further supported by the observation that in the crystal structure of bovine PF4 (58), as in the solution structure of IL-8, the separation between the two helices is about 15 Å and the residues on the N-terminal side of the first cysteine residue are disordered. In this regard, it is also worth noting that modeling studies indicate that the quaternary structure of members of the MCAF/MCP-1 subfamily is likely to be similar to that of the open form of IL-8 on the basis of steric and electrostatic considerations (64). Thus, in the case of MCAF/MCP-1, the carboxylate of Asp-68 (equivalent to Leu-66 of IL-8) of one subunit would be separated by less than 3.5 Å from the carboxylate of Asp-68' of the other when modeled on the basis of the closed form of IL-8, an interaction that would clearly be disfavored electrostatically, in contrast to the model based on the open form where the two negatively charged groups are separated by 5-6 Å. In addition, Arg-

30 (equivalent to Val-27 of IL-8) would clash sterically with the overlying Asp-68' in the closed form, while in the model based on the open form Arg-30 can interact in an electrostatically favorable manner with Glu-39 (equivalent to Thr-37 of IL-8) of its own subunit and Asp-68' of the other. Finally, the hydroxyl group of Tyr-28 (equivalent to Leu-25 of IL-8) would clash with the side chain of Met-64 (equivalent to Val-62 in IL-8), while in the open form it is clearly solvent accessible.

ACKNOWLEDGMENTS

REFERENCES

1. Blundell, T. L., and Johnson, L. N. (1976) Protein Crystallography, Academic Press, New York.

2. Clore, G. M., and Gronenborn, A. M. (1989) *CRC Crit. Rev. Biochem. Mol. Biol.* **24**, 479–564.

3. Clore, G. M., and Gronenborn, A. M. (1991) *Science* **252**, 1390–1399.

4. Dinarello, C. A. (1989) *Adv. Immunol.* **44**, 153–205.

5. Clore, G. M., Wingfield, P. T., and Gronenborn, A. M. (1991) *Biochemistry* **30**, 2315–2323.

6. Fincel, B. C., Clancy, L. L., Holland, D. R., Muchmore, S. W., Watenpaugh, K. D., and Einspahr, H. M. (1989) *J. Mol. Biol.* **209**, 779–791.

7. Priestle, J. P., Schär, H.-P., and Grütter, M. (1989) *Proc. Natl. Acad. Sci. USA* **86**, 9667–9671.

8. Veerapandian, B., Gilliland, G. L., Raag, R., Svensson, A. L., Masui, Y., Hirai, Y., and Poulos, T. L. (1991) *Proteins* **12**, 10–24.

9. Wingfield, P. T., Payton, M., Tavernier, J., Barnes, M., Shaw, A. R., Rose, K., Simona, M. G., Demaczuk, S., Williamson, K., and Dayer, J.-M. (1986) *Eur. J. Biochem.* **160**, 491–497.

10. Gronenborn, A. M., Clore, G. M., Schmeissner, U., and Wingfield, P. T. (1986) *Eur. J. Biochem.* **161**, 37–43.

11. Clore, G. M., and Gronenborn, A. M. (1991) *J. Mol. Biol.* **221**, 47–53.

12. Shaanan, B., Gronenborn, A. M., Cohen, G. H., Gilliland, G. L., Veerapandian, B., Davies, D. R., and Clore, G. M. (1992) *Science* **257**, 961–964.

13. Varley, P., Gronenborn, A. M., Christensen, H., Wingfield, P. T., Pain, R. H., and Clore, G. M. (1993) *Science* **260**, 1110–1113.

14. MacDonald, H. R., Wingfield, P. T., Schmeissner, U., Shaw, A., Clore, G. M., and Gronenborn, A. M. (1986) *FEBS Lett.* **209**, 295–298.

15. Wingfield, P. T., Graber, P., Shaw, A. R., Gronenborn, A. M., Clore, G. M., and MacDonald, H. R. (1989) *Eur. J. Biochem.* **179**, 565–571.

16. Kamogashira, T., Sakaguchi, M., Ohmoto, Y., Mizuno, K., Shimuzu, R., Nagamura, K., Nakai, S., Masui, Y., and Hirai, Y. (1988) *J. Biochem. (Tokyo)* **104**, 837–840.

17. Huang, J. J., Newton, R. C., Horuk, R., Matthew, J. B., Covington, M., Pezzella, K., and Lin, Y. (1987) FEBS Lett. 223, 294–298.

18. Wingfield, P. T., Graber, P., Movva, N. R., Clore, G. M., Gronenborn, A. M., and MacDonald, H. R. (1987) FEBS Lett. 215, 160–164.

19. Mosley, B., Dower, S. K., Gillis, S., and Cosman, D. (1987) Proc. Natl. Acad. Sci. USA 84, 4572–4576.

20. Labriola-Tompkins, E., Chandra, C., Kaffka, K. L., Biondi, D., Graves, B. J., Hatada, M., Madison, V. S., Karas, J., Kilian, P. L., and Ju, G. (1991) Proc. Natl. Acad. Sci. USA 88, 11182–11186.

21. Gehrke, J., Jobling, S. A., Paik, L. S. K., McDonald, B., Rosenwasser, L. J., and Auron, P. E. (1990) J. Biol. Chem. 265, 5922–5925.

22. Ju, G., Campen, C. A., Benjamin, W. R., Labriola-Tompkins, E., Kuras, E., Plocinski, J., Biondi, D., Kaffka, K., Kilian, P. L., Eisenberg, S. P., and Evans, R. J. (1991) Proc. Natl. Acad. Sci. USA 88, 2658–2662.

23. Sims, J. E., and Dover, S. K. (1990) in The Year of Immunology 1989–1990 (Cruse, J. M., and Lewis, R. E., Eds.), Vol. 6, pp. 112–126, Karger, Basel.

24. Paul, W. E., and Ohara, J. (1987) Annu. Rev. Immunol. 5, 429–460.

25. Yokota, T., Arai, N., de Vries, J., Spits, H., Banchereau, J., Zlotnik, A., Rennick, D., Howard, M., Takebe, Y., Miyatake, S., Lee, F., and Arai, K. (1988) Immunol. Rev. 103, 137–187.

26. Finkelman, F. D., Holmes, J., Katonn, I. M., Urban, J. F., Beckmann, M. P., Peik, L. S., Hooley, K. A., Coffman, R. L., Momman, T. R., and Paul, W. E. (1990) Annu. Rev. Immunol. 8, 303–333.

27. Paul, W. E. (1991) Blood 77, 1859–1870.

28. Boulay, L.-L., and Paul, W. E. (1992) J. Biol. Chem. 267, 20525–20528.

29. Golumbek, P. T., Lazenby, A. J., Levitzky, H. I., Jaffee, L. M., Karasuyama, H., Baker, M., and Pardoll, D. M. (1991) Science 254, 713–716.

30. Tepper, R. I., Pattengale, P. K., and Leder, P. (1992) Cell 57, 503–510.

31. Tepper, R. I., Coffman, R. L., and Leder, P. (1992) Science 257, 548–551.

32. Kühn, R., Rajewski, K., and Muller, W. (1991) Science 254, 707–710.

33. Powers, R., Garrett, D. S., March, C. J., Frieden, E. A., Gronenborn, A. M., and Clore, G. M. (1992) Science 256, 1673–1677.

34. Smith, L. J., Redfield, C., Boyd, J., Lawrence, G. M. P., Edwards, R. G., Smith, R. A. G., and Dobson, C. M. (1992) J. Mol. Biol. 224, 899–904.

35. Powers, R., Garrett, D. S., March, C. J., Frieden, E. A., Gronenborn, A. M., and Clore, G. M. (1993) Biochemistry 32, 6744–6762.

36. Wlodawer, A., Pavlosky, A., and Gutschina, A. (1992) FEBS Lett. 309, 59–64.

37. Walter, M. R., Cook, W. J., Zhao, B. G., Cameron, R. P., Ealick, S. E., Walter, R. L., Reichert, P., Nagabhushan, T. L., Trotta, P. P., and Bugg, C. E. (1992) J. Biol. Chem. 29, 20371–20376.

38. Redfield, C., Boyd, J., Smith, L. J., Smith, R. A. G., and Dobson, C. M. (1992) Biochemistry 31, 10431–10437.

39. De Vos, A. M., Ultsch, M., and Kossiakoff, A. M. (1992) Science 255, 306–312.

40. Abdel-Meguid, S. S., Shiel, H.-S., Smith, W. W., Dayringer, H. E., Violand, B. N., and Bentle, L. A. (1987) Proc. Natl. Acad. Sci. USA 84, 6434–6437.

41. Diedrichs, K., Boone, T., and Karplus, P. A. (1991) Science 254, 1779–1782.

42. Walter, M. R., Cook, W. J., Ealick, S. E., Nagabhushan, T. L., Trotta, P., and Bugg, C. E. (1992) J. Mol. Biol. 224, 1075–1085.

43. Bazan, J. F. (1992) Science 257, 410–412.

44. McKay, D. B. (1992) Science 257, 412–413.

45. Pandit, J., Bohm, A., Jancarik, J., Halenbeck, R., Koths, K., and Kim, S.-H. (1992) Science 258, 1358–1362.

46. Cunningham, B. C., Ultsch, M., De Vos, A. M., Mulkerrin, M. G., Clauser, K. R., and Wells, J. A. (1991) Science 254, 821–825.

47. Fuh, G., Cunningham, B. C., Fukunaga, R., Nagata, S., Goeddel, D. V., and Wells, J. A. (1992) Science 256, 1677–1680.

48. Kaushanksy, K., Shoemaker, S. G., Alfaro, S., and Brown, C. (1989) Proc. Natl. Acad. Sci. USA 82, 1213–1217.

49. Lopez, A. F., Shannon, M. F., Herces, T., Nicola, N. A., Cambareri, B., Dottore, M., Layton, M. J., Eglinton, J., and Vada, M. A. (1992) EMBO J. 11, 909–916.

50. Kruse, N., Tony, H.-P., and Sebald, W. (1992) EMBO J. 11, 3237–3244.

51. Shoemaker, K. R., Kim, P. S., York, E. J., Stewart, J. M., and Baldwin, R. L. (1987) Nature 326, 563–567.

52. Clore, G. M., Appella, E., Yamada, M., Matsushima, K., and Gronenborn, A. M. (1989) J. Biol. Chem. 264, 18907–18911.

53. Clore, G. M., and Gronenborn, A. M. (1992) in Interleukin-8 and Related Chemotactic Cytokines (Baggiolini, M., and Sorg, C., Eds.), Vol. 4, pp. 18–40, Karger, Basel.

54. Matsushima, K., and Oppenheim, J. (1989) Cytokine 1, 2–13.

55. Wolpe, S. D., and Cerami, A. (1989) FASEB J. 3, 2565–2573.

56. Clore, G. M., Appella, E., Yamada, M., Matsushima, K., and Gronenborn, A. M. (1990) Biochemistry 29, 1689–1696.

57. Baldwin, E. T., Weber, I. T., St. Charles, R., Xuan, J.-C., Appella, E., Yamada, M., Matsushima, K., Edwards, B. F. P., Clore, G. M., Gronenborn, A. M., and Wlodawer, A. (1991) Proc. Natl. Acad. Sci. USA 88, 502–506.

58. St. Charles, R., Walz, D. A., and Edwards, B. F. P. (1989) J. Biol. Chem. 264, 2092–2099.

59. Clore, G. M., and Gronenborn, A. M. (1991) J. Mol. Biol. 217, 611–620.

60. Shiffer, M., Ainsworth, C., Xu, Z.-B., Carperos, W., Olsen, K., Solomon, A., Stevens, F. V., and Chang, C.-H. (1989) Biochemistry 28, 4066–4072.

61. Weber, I. T., and Steitz, T. A. (1987) J. Mol. Biol. 198, 311–326.

62. Faber, H. R., and Matthews, B. W. (1990) Nature 348, 263–266.

63. Brennan, R. G., Roderick, S. L., Takeda, Y., and Matthews, B. W. (1990) Proc. Natl. Acad. Sci. USA 87, 8165–8169.

64. Gronenborn, A. M., and Clore, G. M. (1991) Prot. Eng. 4, 263–269.

65. Bjorkman, P. J., Saper, M. A., Samraoui, B., Bennet, S. W., Strominger, J. L., and Wiley, D. C. (1987) Nature 329, 506–512.

66. Bjorkman, P. J., Saper, M. A., Samraoui, B., Bennet, S. W., Strominger, J. L., and Wiley, D. C. (1987) Nature 329, 512–518.

67. Beall, C. J., Mahajan, S., and Kolattukudy, P. E. (1992) J. Biol. Chem. 267, 3455–3459.

68. Leonard, E. J., Yoshimura, T., Walz, A., Baggiolini, M., Walz, D. A., Goetzl, E. J., and Castor, C. W. (1991) J. Leukocyte Biol. 49, 258–265.

69. Kraulis, P. J. (1991) J. Appl. Crystallogr. 24, 946–950.